

Politecnico di Torino

Master's Degree in Biomedical Engineering

A 200 kHz Inductive Wireless Power Receiver for Active Implantable Medical Devices

Supervisors

Prof. Paolo Motto Ros
M.Sc. Andrea Dentis

Candidate

Martina Retico

September 2026

Abstract

Wireless Power Transfer (WPT) is emerging as a promising technology for powering Active Implantable Medical Devices (AIMDs), offering advantages in terms of absence of wired connections, miniaturization, safety and system integration.

This thesis focuses on the design and development of a high-efficiency Receiver (RX) circuit for a Near-Field Inductive Coupling (NIC) WPT system, operating at a low resonant frequency of 200kHz. The WPT system is intended to wirelessly power an implanted bidirectional peripheral nervous system interface (RHS2116), designed for the control of an upper limb mechatronic exoprosthetic. The overall architecture of the WPT system consists of a Transmitter (TX) circuit integrated within the prosthetic socket and the receiver implanted in the patient's arm.

The main design challenges include the need to meet miniaturization requirements imposed by implantations constrains and to maintain efficient power transfer under coil misalignment conditions, which can occur due to patient movements or prosthetic shifting. Furthermore, the WPT system must meet the power demands of the load, by delivering a stable dual-rail supply ($\pm$3.3 V) for neural stimulation, other than a regulated +3.3 V main power supply.

The proposed WPT system operates at a low resonant frequency of 200kHz. This specific frequency was selected to minimize tissue absorption, reduce electromagnetic interference with nearby electronics, and ensure compliance with biomedical safety constraints.

The receiver circuit was designed and simulated in LTspice to optimize the efficiency of the inductive link in supplying the load, varying the coupling conditions to simulate potential misalignments between the coils. Various architectural topologies were evaluated and simulated, while component selection and design optimization were carried out to satisfy the electrical, dimensional, and efficiency requirements.

The circuit simulations led to a final design which offered satisfactory performance, with a power-transfer efficiency of approximately 82% across the inductive link and an overall system efficiency of approximately 65%. These results led to the design of the receiver Printed Circuit Board (PCB) using Altium Designer, validated through dedicated testing.

Contents

List of Tables 4

List of Figures 6

List of Acronyms 7

1 Introduction 9

2 State of Art 11
2.1 Active Implantable Medical Devices . . . 11
2.2 NerveRepack . . . 11
2.3 Wireless Power Transfer systems . . . 12
2.3.1 Resonance frequency . . . 12
2.3.2 Near Field Inductive Coupling . . . 13
2.3.3 WPT architecture . . . 14
2.3.4 Resonant Compensation Topologies . . . 15
2.3.5 Link Efficiency . . . 16
2.4 Maximum Efficiency Point . . . 18
2.5 Safety matters for biomedical applications . . . 18

3 Receiver circuit design 20
3.1 RHS2116 requirements . . . 20
3.1.1 Power Supply Requirements and Rail Configuration . . . 20
3.1.2 Power dissipation . . . 20
3.2 Resonance frequency . . . 25
3.3 Coils characterization . . . 25
3.3.1 Series Resistance at 200 kHz . . . 26
3.4 Resonance Topology Selection . . . 27
3.5 Resonance Capacitance . . . 29
3.6 Matching Network . . . 30
3.7 Voltage Rectifier . . . 31
3.7.1 Diode selection . . . 32
3.8 Power Supply and dual-rial supply generation . . . 32
3.8.1 LTC31291-1 Buck-Boost Converter . . . 33
3.8.2 LTC660 . . . 35

4 Validation through LTspice 36
4.1 Baseline design specifications 36
4.2 Testing 38
4.2.1 Power Consumption 38
4.2.2 Coils Misalignment Analysis 40
4.2.3 Vertical misalignment 41
4.2.4 Angular misalignment 42

5 PCB design and testing 45
5.1 PCB design 45
5.2 Testing 48
5.2.1 LTC4125 DEMO CIRCUIT 2773A-A-KIT 48
5.2.2 Tests setup 49
5.2.3 Stand-Alone Receiver Circuit Investigation 51
5.2.4 Stand-Alone Receiver Rectification Stage Investigation 52

Conclusions and Future Perspectives 54
5.3 Conclusions and Experimental Challenges 54
5.4 Future Perspectives 55

Bibliography 56

List of Tables

3.1 Quiescent currents for different supply levels [15] 21
3.2 System parameters for the NerveRepack project. 23
3.3 Comparison of stimulation parameters reported in selected neural interface studies. 23
3.4 Equivalent load resistances in maximum power conditions. 24
3.5 Equivalent load resistance values for 100 mW, 50 mW, and 30 mW power consumption scenarios. 25
3.6 Electrical properties WE 760308101214 receiver coil [21] 26
3.7 Electrical properties WE 760308101104 transmitter coil [22] 26
3.8 Equivalent series resistance (ESR) of the transmitter and receiver coils. . . 27
3.9 Analytical and simulated performance comparison between SP and SS topologies under identical load conditions. 29
3.10 Simulated stand-alone efficiencies of evaluated rectifier topologies 31
4.1 Power and efficiency performance of the WPT system across the three simulated load conditions. 39
4.2 Average DC input voltage to the DC-DC converter across the simulated load conditions. 40
4.3 Coupling coefficient k as a function of vertical distance D (at $\theta = 0°$). . . . 40
4.4 Coupling coefficient k under combined vertical distance and angular misalignment (θ). 40
4.5 System efficiency as a function of vertical distance D. 41
4.6 Average DC input voltage to the DC-DC converter across different transmission distances. 41
4.7 Correlation between coupling coefficient (k), transmitter current (I_{tx}), receiver voltage (V_{rx}), and DC input voltage ($V_{\mathrm{in,\,DCDC}}$) during LTspice simulations. 42
4.8 System efficiency evaluated at different misalignment angles at a fixed distance of $D = 10\,\mathrm{mm}$. 43
4.9 System efficiency evaluated at different misalignment angles at a fixed distance of $D = 12\,\mathrm{mm}$. 43
4.10 System efficiency evaluated at different misalignment angles at a fixed distance of $D = 14\,\mathrm{mm}$. 43
4.11 System efficiency evaluated at different misalignment angles at a fixed distance of $D = 16\,\mathrm{mm}$. 43

4.12 Average DC input voltage ($V_{\text{in, DCDC}}$) evaluated across different vertical distances and angular misalignments. 44
5.1 Measured parameters for the TX and RX stages. 49
5.2 Comparison between set parameters and actual measured values. 51
5.3 Measured parameters stand-alone recitification stage 53

List of Figures

2.1 NerveRepack project overview [2] . . . 12
2.2 Schematic representation of Near-Field Inductive Coupling (NIC)[3] . . . 13
2.3 General block diagram of an inductive WPT system [9] . . . 14
2.4 L-shaped matching network configurations [11] . . . 15
2.5 Four fundamental resonant compensation topologies for WPT systems: (a)Series-Series (SS) (b)Series-Parallel (SP) (c)Parallel-Series (PS) (d)Parallel-Parallel (PP). . . . 16
2.6 WPT link . . . 18
3.1 Typical biphasic current pulse [15] . . . 22
3.2 Estimated power consuption[20] . . . 24
3.3 Quality factor analysis across frequency for (a) trasmitter coil [22] and (b) receiver coil [21] . . . 27
3.4 Comparison between the (a) SS and (b) SP topologies . . . 28
3.5 SP Resonance configuration . . . 29
3.6 low pass Low-high matching network . . . 30
3.7 Receiver matching network . . . 31
3.8 Full-bridge voltage rectifier . . . 32
3.9 LTC3129-1 buck-boost converter. . . . 34
3.10 LTC660 voltage converter. . . . 35
4.1 LTspice model of the Rx-circuit. . . . 37
4.2 vertical misalignment[29] . . . 41
4.3 angular misalignment[29] . . . 42
5.1 Altium designer schematic . . . 46
5.2 PCB layout . . . 47
5.3 LTC4125 DEMO CIRCUIT 2773A-A-KIT . . . 48
5.4 LTC4125 DEMO CIRCUIT 2773A-A-KIT specifications [30] . . . 48
5.5 Rx circuit test set up . . . 49
5.6 vertical disalignment set up . . . 50
5.7 Rx circuit test set up - stand alone testing . . . 51
5.8 Fluke measurements . . . 52
5.9 PCB - desoldered LTC3129-1 . . . 52
5.10 Test set up - stand-alone rectification stage testing . . . 53

List of Acronyms

AIMDs Active Implantable Medical Devices

WPT Wireless Power Transfer

NIC Near-Field Inductive Coupling

TX Transmitter

RX Receiver

LF Low Frequency

RL Load Resistance

RS Source Resistance

EV Electric Vehicles

SS Series-Series

SP Series-Parallel

PS Parallel-Series

PP Parallel-Parallel

MEP Maximum Efficiency Point

RMS Root Mean Square

PCB Printed Circuit Board

RF Radio Frequency

Chapter 1

Introduction

Wireless Power Transfer (WPT) has emerged as an innovative technology in the design of Active Implantable Medical Devices (AIMDs), offering a definitive solution to the limitations of conventional power delivery. The use of a WPT system eliminates the need for wired electrical connections, which reduces the risk of infections due to surgical implantation and removes the need for battery replacement due to depletion. Furthermore, the use of an external source to transfer energy to the implanted electronics allows to significantly downsize the battery or replace it [1]. Consequently, WPT systems are being increasingly adopted across biomedical applications. Designing an effective WPT link is a complex challenge that requires balancing several important key parameters such as the physical size of the WPT system, the physical distance between the external transmitter and the implanted receiver, the operating frequency, and the thermal safety limits imposed to prevent biological tissue damage from power dissipation [1].

This thesis is developed within the framework of NerveRepack, a European Union co-funded research initiative aimed at engineering a new generation of bidirectional implantable electrodes.The NerveRepack project aim is to connect the human nervous system with external mechatronic structures, such as exoskeletons and exoprosthetics. [2].

Specifically, the primary objective of this work is the design, optimization, and validation of a high-efficiency implantable Receiver (RX) circuit for a Near-Field Inductive Coupling (NIC), dedicated to continuously power the bidirectional peripheral nervous system interface Intan RHS2116, designed for the control of an upper limb mechatronic exoprosthetic.

The choice of an operating frequency of 200 kHz, falling within the Low Frequency (LF) band, is driven by key physiological and electromagnetic considerations. While the literature mostly relies on higher frequencies, such as 13.56 MHz or 6.78 MHz [3], the selection of 200 kHz for this architecture finds justification in the following considerations. From a signal integrity perspective, operating at this frequency allows to mitigate electromagnetic interference with the surrounding electronic components and reduces parasitic capacitive coupling compared to higher frequencies [4]. Furthermore, this frequency is kept well above the threshold of neural and cardiac membrane excitation, which occurs at much lower frequencies, ensuring that the power transfer avoids any stimulation of surrounding nerves or muscles while maintaining stable power management.

The development, modeling and performance evaluation of the proposed WPT system

receiver are presented across the following chapters:

Chapter 2 Illustrates the state of art of WPT systems.

Chapter 3 details the hardware design of the RX circuit. It documents the electrical requirements of the RHS2116 neurostimulator, engineering rationale behind every circuit choice, including the evaluation of different rectifier topologies and the implementation of a dual-rail power management stage utilizing the LTC3129-1 and the LTC660 integrated circuits.

Chapter 4 presents the validation of the proposed system in a simulated environment. It analyzes the circuit's stage-by-stage and total efficiencies under load condition variation and spatial misalignment of the coils.

Finally, Chapter 5 reports the PCB layout design and the empirical results obtained during physical experimental testing, providing a detailed analysis of the experimental challenges encountered.

Chapter 2

State of Art

2.1 Active Implantable Medical Devices

AIMDs are defined as medical devices that rely on an electrical energy source for their operation and are intended to be totally or partially introduced, surgically or medically, into the human body [5]. These devices are primarily designed to electrically stimulate specific organs or tissues or to monitor physiological parameters, by recording biomedical signals.

Among the major challenges associated with AIMDs is the limited lifetime of their internal batteries. Battery depletion inevitably requires additional surgical interventions for replacement, which are invasive, uncomfortable for the patient, and increase the risk of surgical complications. The use of WPT systems is a solution which has been extensively investigated in the literature to overcome these limitations.

WPT can be employed either to periodically recharge an internal battery, as seen in modern pacemakers [4], or to establish a direct wireless inductive power link, eliminating the need for a battery itself , as commonly implemented in cochlear implants [6], or ventricular assist devices [7]. The approach of direct wireless powering is particularly advantageous for devices that require miniaturization and for which the integration of a battery is physically unfeasible.

2.2 NerveRepack

Nerve Repack is an innovative project in the field of neuroprosthetics. The overall aim of this project is to bring innovative revolutions by focusing on the development of implantable interfaces that enable bidirectional communication between the nervous system and external devices. The target is to allow individuals to regain both motor control and sensory feedback, establishing a connection between their nerves and advanced prosthetic limbs or exoskeletons. Nerve Repack is co-fundend by the European Union and it is driven by the desire to improve the quality of life for individuals who deal with amputation or paralysis of the limbs [2].

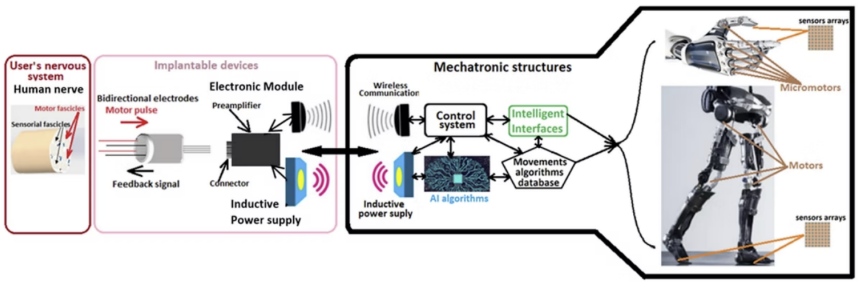


Figure 2.1: NerveRepack project overview [2]

This thesis project is situated within this context, specifically addressing the wireless charging of the bidirectional peripheral nervous system interface Intan RHS2116. Referring to Figure 2.1, the power delivery is achieved through a WPT system with an architecture consisting of two main stages: a TX circuit integrated within the mechatronic structure of the external prosthetic socket, and an RX circuit implemented in the electronic module implanted directly into the patient's arm.

2.3 Wireless Power Transfer systems

WPT allows for the transmission of electrical energy from a power source to a load without relying on physical cables. The primary challenges in designing a highly efficient WPT system include miniaturization constraints due to the implantation site, the spatial separation distance between the external transmitter coil and the implanted receiver coil, the selection of an optimal operating frequency, and compliance with thermal safety regulations to prevent tissue damage induced by power dissipation [1].

2.3.1 Resonance frequency

One of the most critical aspects in the design of a WPT system is the selection of the optimal operating frequency.

- Lower frequencies offer improved magnetic field penetration through biological tissues, which results essential for charging implanted devices. However, studies have shown that overall WPT performance and efficiency can be compromised [4].
- Higher frequencies increase the risk of eddy current losses and localized tissue heating. Furthermore, it can generate electromagnetic compatibility issues within the electronic circuitry of the AIMD. However, in this case, the WPT systems show higher efficiency[4].

Generally, the applicable frequency bands for medical implants span across 133–150 kHz, 13.56 MHz, 868/915 MHz, 2.45 GHz, 5.2 GHz, and 5.8 GHz. In the literature, many inductively powered biomedical systems are designed to resonate at 13.56 MHz, or within other Industrial, Scientific, and Medical (ISM) bands such as 6.78 MHz, mainly for practical reasons, since numerous off-the-shelf components are optimized for the frequency of

13.56 MHz [3]. Furthermore, operating within the 1–13 MHz range provides a balance between maximizing the transferred power and adhering to electromagnetic safety limits concerning tissue absorption [8].

2.3.2 Near Field Inductive Coupling

WPT systems are generally devided in near-field and far-field links, and this classification is based on thier working princle. In far-field links, the energy is transported by and electromagnetic wave, while in near-field links by magnetic or electric coupling. [9].

NIC is commonly used to transfer power to implanted bioelectronic devices due to the fact that magnetic fields at these frequencies can pass through tissue from a small distance away with little or no attenuation.

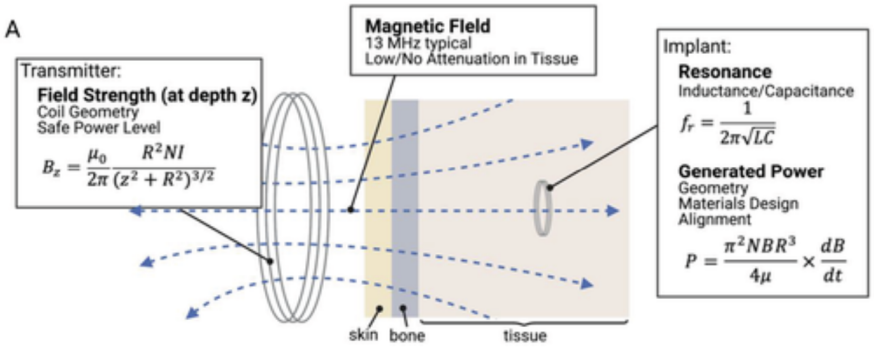


Figure 2.2: Schematic representation of Near-Field Inductive Coupling (NIC)[3]

Figure 2.2 shows an schematic representation of NIC: an external transmitting coil inductively powers an implanted receiving coil through the generation of alternating magnetic fields.

The field strength at a distance z from the center of the coil is given by 2.1

$$B_z = \frac{\mu_0}{2\pi} \frac{R^2 NI}{(z^2 + R^2)^{3/2}} \tag{2.1}$$

where R represents the radius of the coil, N the number of turns in the coil, and I the current through the coil. These three factors can be optimized for the specific application.

In NIC the magnetic field induces a voltage and current that is proportional to the magnetic flux captured by the coil. The power generated by an inductively powered coil depends on its area, the number of turns N, and the strength of the magnetic field B. For a circular coil geometry, the power received at the receiver coil can be written as 2.2.

$$P = \frac{\pi^2 NBR^3}{4\mu} \times \frac{dB}{dt} \tag{2.2}$$

Another important consideration is the resonant frequency f_r (2.3), for which power transfer is maximized. For NIC this resonance is determined by the inductance of the coil (L) and the total capacitance of the receiver (C), which is tuned by changing the value of the resonance capacitor in the circuit [3].

$$f_r = \frac{1}{2\pi\sqrt{LC}} \tag{2.3}$$

2.3.3 WPT architecture

The general block diagram of an inductive WPT system is illustrated in Figure 2.3.

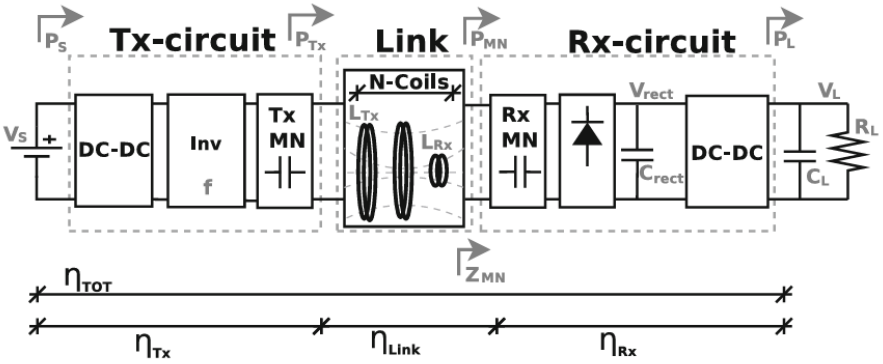


Figure 2.3: General block diagram of an inductive WPT system [9]

The TX circuit drives an AC current through the TX coil, which magnetically induces an AC voltage across the RX coil. The RX circuit conditions this induced voltage to supply the load.

Since the primary focus of this work is the development of the receiver, the following discussion will concentrate exclusively on the RX circuit design. An overview of its functional blocks follows:

- Inductive Link: This stage transfers power through an alternating magnetic field operating at the system's carrier frequency. The inductive link comprises the TX coil and the RX coil, and its overall performance is characterized by the link efficiency (η_{link}), which will be detailed in Section 2.3.5.

  The fundamental elements governing the WPT are the coils themselves, which are defined by their respective self-inductances, L_{tx} and L_{rx}. When an alternating current is driven through the TX coil, it generates a magnetic flux. A portion of this flux links with the RX coil, establishing a magnetic interaction quantified by the mutual inductance (M).

  The effectiveness of this magnetic link is expressed by the coupling coefficient (k), which is an adimensionale value, ranging from 0 (indicating completely uncoupled coils) to 1 (representing perfect, leakage-free magnetic coupling), is mathematically defined as expressed in Equazion 2.4 [9]:

$$k = \frac{M}{\sqrt{L_{\text{tx}} L_{\text{rx}}}} \tag{2.4}$$

- Rx Matching Network: This stage matches the impedance of the receiver coil to the following stages of the receiver circuit in order to maximize the overall link efficiency. Specifically, it is designed to cancel the reactive component of the RX coil, thereby achieving resonance [9]. Various matching network topologies are documented in the literature, including the L-match, π-match, and T-match configurations [10].

  In particular, the L-match is the simplest configuration used to match the impedance between a source and a load. The placement of its reactive components depends on the resistance values: if the Load Resistance (RL) is greater than the Source Resistance (RS), a shunt element must be placed in parallel with the load. Conversely, if $R_L < R_S$, a series element is connected to the load. The four primary L-match configurations are illustrated in Figure 2.4.

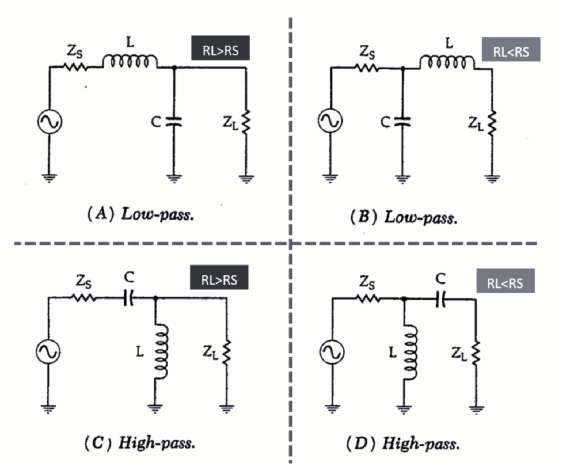


Figure 2.4: L-shaped matching network configurations [11]

  A simple series or parallel compensation capacitor, which is utilized to achieve resonance at the receiver, can be considered a special case of the L-match network where one of the reactive components has either zero (short circuit) or infinite (open circuit) impedance [9].

- Rectifier: This stage is required to provide a DC voltage to the following DC-DC converter by rectifying the input AC signal.

- DC-DC Converter: This stage ultimately regulates the output voltage to the precise values required by the project specifications.

2.3.4 Resonant Compensation Topologies

Figure 2.5 illustrates the four fundamental resonant compensation architectures commonly employed in WPT systems. Among these, the configurations featuring a voltage source with a series resonant capacitor at the transmitter (Figures 2.5a and 2.5b) are the most widely adopted [9].

The characteristics of each configuration are summarized below:

- SS: This architecture is driven by a voltage source at the TX. It is generally the preferred choice for high-power applications, such as wireless charging systems for Electric Vehicles (EV), where the RL is on the same order of magnitude as R_{rx} [9].
- SP: This architecture is also driven by a voltage source at the TX, and is suited for low-power applications, including AIMDs, where the equivalent RL is significantly larger than R_{rx} [9].
- PS: This architecture is driven by a current source at the TX. Similar to the SS topology, it is typically implemented in high-power systems where the RL is on the same order of magnitude as R_{rx} [9].
- PP: This architecture is driven by a current source at the TX,and is results optimal for low-power applications where the RL is significantly larger than R_{rx} [9].

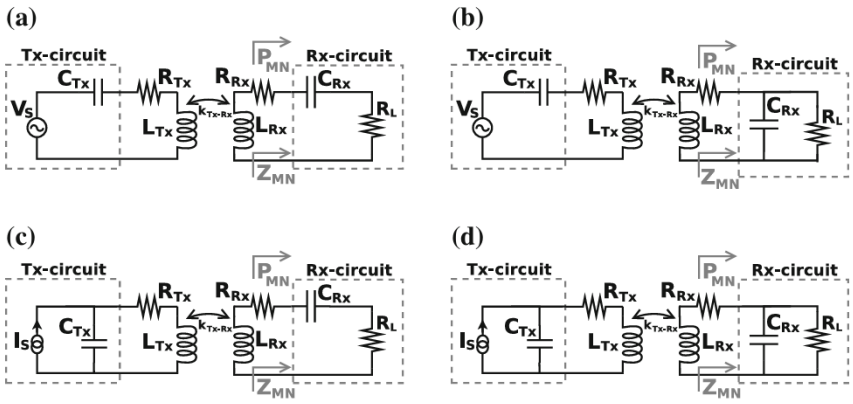


Figure 2.5: Four fundamental resonant compensation topologies for WPT systems: (a)SS (b)SP (c)PS (d)PP.

2.3.5 Link Efficiency

When evaluating the performance of the inductive link, the most critical parameter to consider is the link efficiency (η_{Link}), which is given by:

$$\eta_{\text{Link}} = \frac{Q_{\text{Rx-L}}}{Q_L} \frac{k^2_{\text{Tx-Rx}} Q_{\text{Tx}} Q_{\text{Rx-L}}}{k^2_{\text{Tx-Rx}} Q_{\text{Tx}} Q_{\text{Rx-L}} + 1} \tag{2.5}$$

where $k_{\text{Tx-Rx}}$ is the coupling coefficient between the transmitter and receiver coils, previously introduced in Section 2.3.3. This coefficient is highly dependent on the vertical separation distance D, the radii of the transmitting and receiving coils (r_{Tx} and r_{Rx}, respectively), and the relative orientation defined by θ, which denotes the angular misalignment. The analytical expression for the coupling coefficient $k_{\text{Tx-Rx}}$ is [12]:

$$k_{\text{Tx-Rx}} = \frac{r^2_{\text{Tx}} r^2_{\text{Rx}} \cos(\theta)}{\sqrt{r_{\text{Tx}} r_{\text{Rx}}} \left(\sqrt{D^2 + r^2_{\text{Tx}}}\right)^3} \tag{2.6}$$

Furthermore, $Q_{\text{Rx-L}}$ is the equivalent quality factor of the receiver and the load, expressed as:

$$Q_{\text{Rx-L}} = \frac{Q_{\text{Rx}} Q_L}{Q_{\text{Rx}} + Q_L} \tag{2.7}$$

where Q_{Rx} is the quality factor of the RX coil, defined as:

$$Q_{\text{Rx}} = \frac{\omega L_{\text{Rx}}}{R_{\text{Rx}}} \tag{2.8}$$

Here, $\omega = 2\pi f$ is the angular operating frequency, L_{Rx} is the inductance of the receiving coil, and R_{Rx} is its equivalent series resistance.

Finally, Q_L represents the equivalent quality factor of the load:

$$Q_L = \frac{\omega L_{\text{Rx}}}{\text{Re}\{Z_{\text{MN}}\}} \tag{2.9}$$

where $\text{Re}\{Z_{\text{MN}}\}$ is the real part of the matching network impedance (Figure 2.3).

2.4 Maximum Efficiency Point

In the design of a WPT system, reaching the optimum operating point corresponds to maximizing the overall efficiency. Generally, efficiency is maximized when $\Im\{Z_{\text{mn}}\} = -\omega L_{\text{rx}}$, which defines the RX resonance condition. Regarding the real part, $\Re\{Z_{\text{mn}}\}$ (Figure 2.6), two optimal values exist depending on whether the objective is to maximize the link efficiency or the power delivered to the load (P_{MN}). For the purposes of this study, the design of the rectifier proceeded by prioritizing the link efficiency to achieve the Maximum Efficiency Point (MEP).

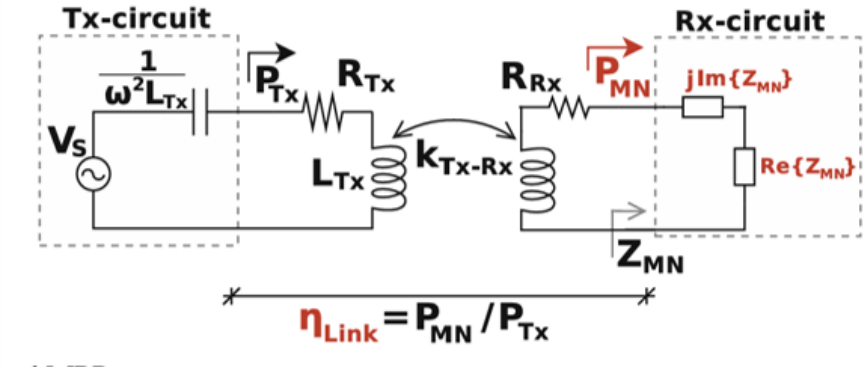


Figure 2.6: WPT link

The following equations were taken into consideration [9]: The theoretical maximum link efficiency is achieved by configuring the receiver load to match the optimal impedance ($Z_{MN_{opt-\eta}}$), which is calculated as follows:

$$Re\{Z_{MN_{opt-\eta}}\} = R_{Rx}\sqrt{k^2_{Tx-Rx}Q_{Tx}Q_{Rx} + 1}. \tag{2.10}$$

The maximum value of the link efficiency is given by:

$$\eta_{\text{link,max}} = \frac{k^2_{\text{Tx-Rx}}Q_{\text{Tx}}Q_{\text{Rx}}}{\left(\sqrt{k^2_{\text{Tx-Rx}}Q_{\text{Tx}}Q_{\text{Rx}} + 1} + 1\right)^2}. \tag{2.11}$$

A matching network can be used to adjust ZMN, achieving resonance or the MEP.

2.5 Safety matters for biomedical applications

Because the receiver is intended for implantation within human tissue, rigorous anatomical and safety constraints must be considered:

- Electromagnetic Field and SAR Limits: The generated electromagnetic fields must comply with the Specific Absorption Rate (SAR) limits established by ICNIRP guidelines. The Federal Communications Commission (FCC) limits the maximum averaged SAR to 1.6 W/kg, measured over 1 g of tissue mass during 6 minutes of exposure [8]. The SAR is mathematically defined as:

$$SAR = \frac{\sigma |E_{\text{rms}}|^2}{\rho} \tag{2.12}$$

where E_{rms} is the root mean square value of the electric field, σ is the tissue conductivity, and ρ is the tissue density.

According to Maxwell's equations (specifically Faraday's law of induction), the induced electric field E can be derived from the time-varying magnetic field B as follows:

$$\nabla \times E = -\frac{\partial B}{\partial t} \propto \omega_p I_1 \tag{2.13}$$

where ω_p is the operating angular frequency and I_1 is the current flowing through the transmitter. This relationship highlights a fundamental design trade-off in inductive links: it is possible to safely increase the external driving current, therefore improve the magnetic field strength for deeper tissue penetration, while keeping the SAR constant, simply by decreasing the operating frequency of the system [13].

- Miniaturization: The anatomical location imposes physical implantation challenges. The receiver coil circuit must be miniaturized to respect the implantation site, minimizing surgical invasiveness and patient discomfort.
- Thermal Constraints and Power Dissipation: AIMDs must manage heat generation to prevent thermal damage to the surrounding biological tissue. The RX circuit must ensure low power dissipation to prevent dangerous heat accumulation.
- Biocompatible Materials and Packaging: The long-term safety of the system depends on the encapsulation of the electronic components. Biocompatible materials must be used to shield the patient's tissues from toxic materials and protect the sensitive implanted circuitry from the corrosive environment of bodily fluids.

Chapter 3

Receiver circuit design

3.1 RHS2116 requirements

3.1.1 Power Supply Requirements and Rail Configuration

To optimally design the receiver of the WPT system, the specific electrical power requirements of the load must be defined.

For biological integration, the RHS2116 supports biphasic stimulation and passive charge balancing. These functionalities are necessary to ensure tissue safety, prevent localized charge accumulation, and maintain the long-term electrochemical integrity of the electrode-tissue interface [14].

To support the complex neuro-stimulation tasks, the WPT receiver must be capable of providing a stable, multi-rail voltage supply. The specific operational requirements of the RHS2116 are defined as follows:

- Logic and Analog Supply (VDD): The core operations, including the recording amplifiers and digital logic, require a nominal stable positive supply of +3.3V.
- Positive Stimulation Rail (VSTIM+): The internal constant-current stimulators require a dedicated positive rail, which must be tied to a voltage within the range of +3.3V to +7.0V.
- Negative Stimulation Rail (VSTIM-): To enable the negative current phase of the biphasic stimulation pulses, a symmetrical negative power supply ranging from -3.3V to -7.0V is required [15].

For the specific scope of this thesis, the stimulation rails considered were ± 3.3 V, as specified in the Nerverepack project specifications.

3.1.2 Power dissipation

The total power dissipation of the Intan Technologies RHS2116 chip depends on its configuration. To design properly the receiver circuit, the current drawn from each supply rail was evaluated in order to define equivalent load resistances. These resistances reflect the

load imposed by the RHS2116, ensuring that the simulation models correctly emulate the chip's behavior under the operating conditions.

The overall current consumption of this device is not a constant value, but it comprises a fixed quiescent baseline and dynamic components that scale as a function of the recording settings.

The quiescent current drawn from the +3.3 V V_{DD} supply, according to technical specifications [15], is composed of a fixed baseline current of 3.2 mA (I_{baseline}) to power various voltage references, bias current generators, and ADC circuitry. To this, a 5.7 mA load for the LVDS I/O transceiver (I_{LVDS}) and 0.12 mA for the impedance measurement module ($I_{\mathrm{imp_meas}}$) must be added. The dynamic recording consumption scales proportionally with bandwidth and channel count, applying specific coefficients: 9.2 μA/kHz per active AC amplifier and 5.2 μA/(kS/s) for the ADC/MUX block. The total quiescent logic current (I_{VDD_quies}) is formulated as follows:

$$\begin{aligned} I_{\mathrm{VDD_quies}} = {} & I_{\mathrm{baseline}} + I_{\mathrm{LVDS}} + I_{\mathrm{imp_meas}} \\ & + N_{\mathrm{rec}} \left(9.2 \, \frac{\mu\mathrm{A}}{\mathrm{kHz}} \cdot f_H + 5.2 \, \frac{\mu\mathrm{A}}{\mathrm{kS/s}} \cdot f_{\mathrm{sample_ch}} \right) \end{aligned} \tag{3.1}$$

Besides the standard +3.3 V V_{DD} supply, the RHS2116 circuits require dedicated rails (V_{STIM+} and V_{STIM-}). Even when no stimulation pulses are actively generated, these rails draw quiescent currents that depend on the selected voltages (Table 3.1).

VSTIM±	supply current from VSTIM+	supply current from VSTIM–
±3.3V	0.57 mA	0.41 mA
±6.0V	0.61 mA	0.46 mA
±7.0V	0.62 mA	0.48 mA
+3.3V / -10.7V	0.57 mA	0.51 mA
+10.7V / -3.3V	0.64 mA	0.41 mA

Table 3.1: Quiescent currents for different supply levels [15]

As specified in Section 3.1.1, the stimulation rails are ±3.3 V, and consequently, the quiescent currents are 0.57 mA and 0.41 mA for the positive and negative rails, respectively.

The current related to stimulation consumption was then evaluated considering biphasic stimulation pulses, as shown in Figure 3.1

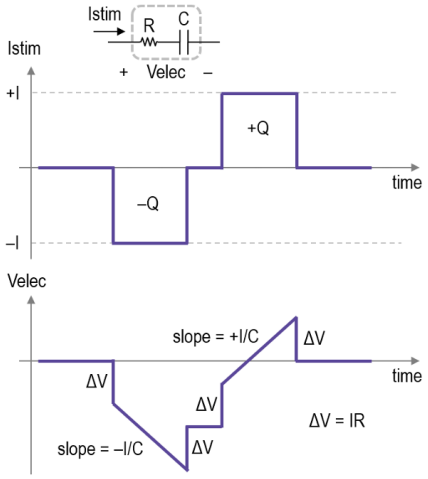


Figure 3.1: Typical biphasic current pulse [15]

Impulse width, T, values are in a range from $T_{\mathrm{MIN}} = 20\,\mu\mathrm{s}$ to $T_{\mathrm{MAX}} = 1\,\mathrm{ms}$. The duty cycle of the stimulation signal was defined as:

$$D = f_{\mathrm{stim}}(T_1 + T_2) \tag{3.2}$$

where f_{STIM} is the stimulation frequency, while T_1 and T_2 represent the durations of the negative and positive stimulation phases, respectively.

Through a time-weighted averaging procedure the instantaneous currents for the positive and negative stimulation phases were converted into average values.

If a positive stimulation current with magnitude I_{STIM} is supplied from one channel, the currents drawn from each power supply increase during stimulation as follows [15]:

$$V_{\mathrm{DD}}: \quad \Delta I = 0.23 \cdot I_{\mathrm{STIM}} \tag{3.3}$$
$$V_{\mathrm{STIM+}}: \quad \Delta I = 1.15 \cdot I_{\mathrm{STIM}} \tag{3.4}$$
$$V_{\mathrm{STIM-}}: \quad \Delta I = 0 \tag{3.5}$$

If a negative stimulation current is supplied from one channel, the current increases by the stimulation:

$$V_{\mathrm{DD}}: \quad \Delta I = 0.10 \cdot I_{\mathrm{STIM}} \tag{3.6}$$
$$V_{\mathrm{STIM+}}: \quad \Delta I = 0.34 \cdot I_{\mathrm{STIM}} \tag{3.7}$$
$$V_{\mathrm{STIM-}}: \quad \Delta I = 1.31 \cdot I_{\mathrm{STIM}} \tag{3.8}$$

I_{STIM} values are in a range from $I_{\mathrm{STIM,\,MIN}} = 2.55\,\mu\mathrm{A}$ to $I_{\mathrm{STIM,\,MAX}} = 2.5\,\mathrm{mA}$, according to [15].

The average stimulation current was therefore obtained as:

$$I_{\mathrm{avg}} = \frac{T_1}{T_1 + T_2} I_{\mathrm{neg}} + \frac{T_2}{T_1 + T_2} I_{\mathrm{pos}} \tag{3.9}$$

Considering the pulsed operation of the chip, the resulting average value was then multiplied by the duty cycle. The total current drawn from each supply rail was calculated by summing the contributions of the quiescent and stimulation currents. Finally, the overall power consumption of the system was calculated as:

$$P_{\text{tot}} = V_{\text{DD}} I_{\text{DD,tot}} + V_{\text{STIM}} I_{\text{VSTIM+,tot}} + V_{\text{STIM}} I_{\text{VSTIM−,tot}} \tag{3.10}$$

Table 3.2 reports the parameters related to the Nerverepack project

Parameter	**Value**
ch_{stim}	2
ch_{rec}	5
V_{stim}	3.3 V
f_H	5 kHz
$f_{\text{sample,ch}}$	10 kS/s/channel

Table 3.2: System parameters for the NerveRepack project.

Different studies including RHS2116 were considered [16, 17, 18, 19], and summarized in Table 3.3.

Article	**Waveform**	**Frequency (f)**	**Pulse Width**
Wright *et al.* [16]	Biphasic	30 Hz	1000 μs (range: 100–1000 μs)
Lienemann *et al.* [17]	Biphasic pulse trains	1 Hz	200 μs
Zurita *et al.* [18]	Bipolar	1 Hz	500 μs
Carnicer-Lombarte *et al.* [19]	Trains of 100 biphasic pulses	100 Hz (10 ms period)	100 μs

Table 3.3: Comparison of stimulation parameters reported in selected neural interface studies.

$f_{\text{STIM}} = 30$ Hz was chosen, to evaluate the worst case [16].

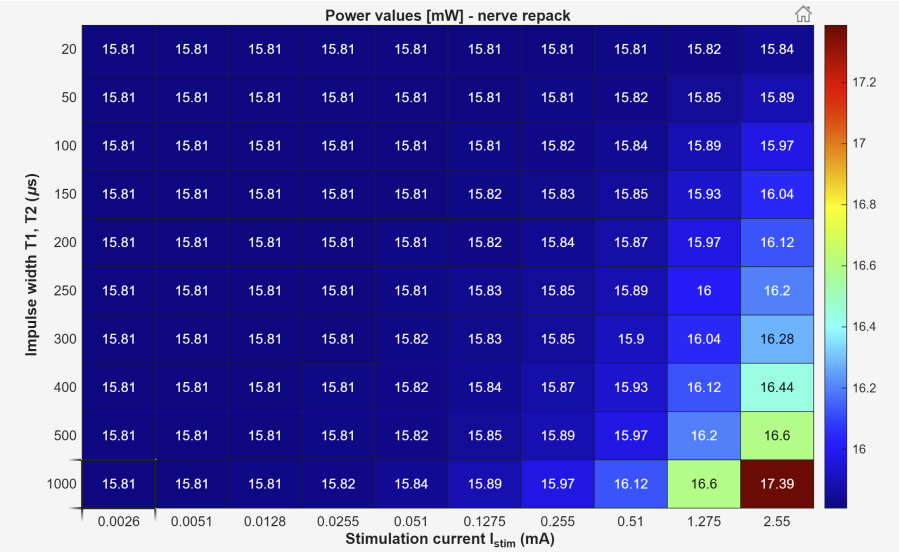


Figure 3.2: Estimated power consuption[20]

In reference to the colormap in Figure 3.2, the maximum power consumption is equal to $P_{\mathrm{MAX}} = 17.39\,\mathrm{mW}$, which corresponds to the highest stimulation current and pulse width ($I_{\mathrm{STIM}} = 2.55\,\mathrm{mA}$ and $T_1 = T_2 = 1000\,\mu\mathrm{s}$). These values were used to compute the equivalent resistances:

$$R_{\mathrm{vdd}} = \frac{V_{\mathrm{dd}}}{I_{\mathrm{vdd,tot}}} \tag{3.11}$$

$$R_{\mathrm{vstim+}} = \frac{V_{\mathrm{stim}}}{I_{\mathrm{vstim+,tot}}} \tag{3.12}$$

$$R_{\mathrm{vstim-}} = \frac{V_{\mathrm{stim}}}{I_{\mathrm{vstim-,tot}}} \tag{3.13}$$

Parameter	Value
$R_{V_{\mathrm{DD}}}$	$854.81\,\Omega$
$R_{V_{\mathrm{STIM+}}}$	$4135.49\,\Omega$
$R_{V_{\mathrm{STIM-}}}$	$5406.03\,\Omega$

Table 3.4: Equivalent load resistances in maximum power conditions.

In a fully integrated implantable system, the wireless power transfer (WPT) link must realistically supply power not only to the neural stimulation chip but also to an onboard microcontroller unit (MCU). To account for this overall power demand, three distinct consumption conditions were selected to evaluate the circuit's performance. Table 3.5 presents the equivalent load resistance values for the 100 mW, 50 mW, and 30 mW scenarios, which correspond to the maximum, typical, and minimum operating states of the device,

respectively. The equivalent load resistance values were calculated by scaling the baseline parameters previously defined in Table 3.4.

Parameter	100 mW Scenario	50 mW Scenario	30 mW Scenario
R_{vdd}	148.65 Ω	297.3 Ω	495 Ω
$R_{\text{vstim+}}$	719.16 Ω	1438.3 Ω	2394 Ω
$R_{\text{vstim-}}$	940.1 Ω	1880 Ω	3130 Ω

Table 3.5: Equivalent load resistance values for 100 mW, 50 mW, and 30 mW power consumption scenarios.

3.2 Resonance frequency

Although a vast body of literature focuses on inductively powered systems designed to resonate within unlicensed Industrial, Scientific, and Medical (ISM) bands, most notably at 13.56 MHz or 6.78 MHz [3], the selection of a 200 kHz LF carrier for this specific neurostimulator application is strongly justified by several critical factors regarding biological safety and signal integrity, which were already exposed in Section 2.3.1.

3.3 Coils characterization

Due to the application, there are strict constraints on the physical dimension of the coils. This is especially critical for the receiver coil, which must be sufficiently miniaturized to allow the implantation within the human arm, while the transmitter coil's size is constrained by the geometry of the socket. Furthermore, the coils must be suitable to resonate efficiently at the system's target operating frequency of 200kHz. Two commercial off-the-shelf coils were selected for this purpose:

- Receiver (RX) Coil: WE 760308101214 (diameter: 19 mm; thickness: 0.8 mm)
- Transmitter (TX) Coil: WE 760308101104 (diameter: 20 mm; thickness: 2.8 mm)

The electrical properties of these components, as provided by the manufacturer, are summarized in Table 3.6 and Table 3.7.

Electrical Properties:

Properties		Test conditions	Value	Unit	Tol.
Inductance	L	125 kHz/ 10 mA	26	µH	±10%
Rated Current	I_R	ΔT = 40 K	1.1	A	max.
Q-Factor	Q	125 kHz/ 10 mA	25		typ.
Power Capability	P	V_{DC} = 20 V	20	W	typ.
DC Resistance	R_{DC}	@ 20 °C	420	mΩ	typ.
DC Resistance	R_{DC}	@ 20 °C	520	mΩ	max.
Self Resonant Frequency	f_{res}		11	MHz	typ.

Table 3.6: Electrical properties WE 760308101214 receiver coil [21]

Electrical Properties:

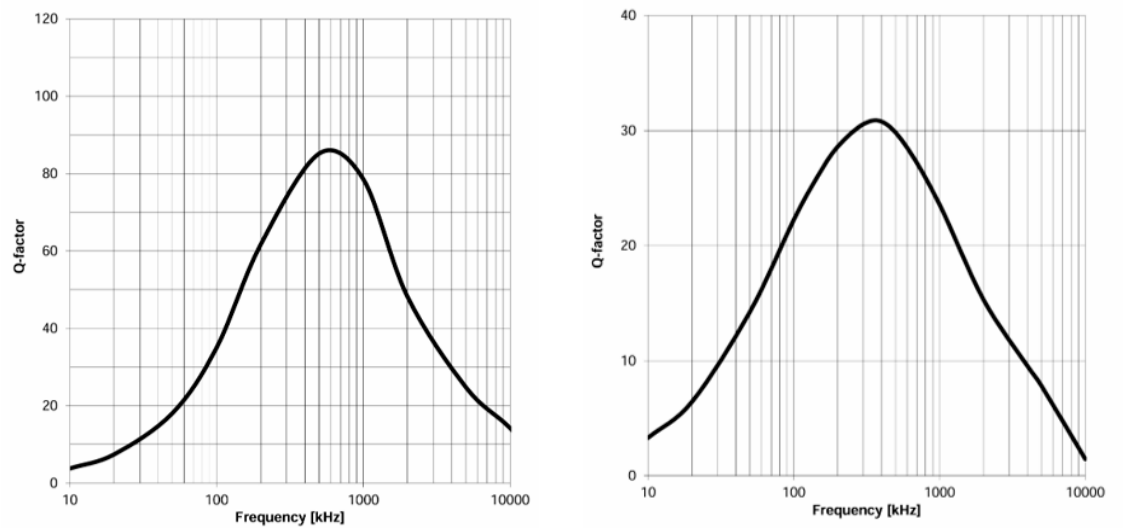
Properties		Test conditions	Value	Unit	Tol.
Inductance	L	125 kHz/ 10 mA	6.8	µH	±10%
Q-Factor	Q	125 kHz/ 10 mA	42		typ.
Power Capability	P	V_{DC} = 20 V	50	W	typ.
Rated Current	I_R	ΔT = 40 K	2.5	A	max.
DC Resistance	R_{DC}	@ 20 °C	110	mΩ	typ.
DC Resistance	R_{DC}	@ 20 °C	130	mΩ	max.
Self Resonant Frequency	f_{res}		20	MHz	typ.

Table 3.7: Electrical properties WE 760308101104 transmitter coil [22]

3.3.1 Series Resistance at 200 kHz

The Equivalent Series Resistance (ESR) of both coils at the 200 kHz operating frequency was derived by evaluating their respective quality factors (Q-factors), as illustrated in the plots of Figure 3.3.

$$Q = \frac{\omega L}{R_s} \implies R_s = \frac{2\pi f L}{Q} \tag{3.14}$$



(a) (b)

Figure 3.3: Quality factor analysis across frequency for (a) trasmitter coil [22] and (b) receiver coil [21]

The results obtained are shown in Table 3.8:

Coil	**Parameter**	**Equivalent Series Resistance**
Transmitter	R_{tx}	142 mΩ
Receiver	R_{rx}	1.167 Ω

Table 3.8: Equivalent series resistance (ESR) of the transmitter and receiver coils.

3.4 Resonance Topology Selection

Although SS resonant topology is the most prevalent topology in WPT literature, a comparative analysis was conducted during the design phase to determine the optimal architecture for this specific application. Both SS and SP configurations were analyzed under identical power emission and load conditions.

According to the inductive link theory previously discussed in Section 2.3.4, the SP topology is generally preferred for AIMDs. Furthermore, studies have demonstrated that at frequencies close to 200 kHz, the SP configuration yields superior performance in terms of efficiency compared to the SS configuration [4].

The following evaluations have been performed:

- Analytical Evaluation: A preliminary theoretical calculation of the expected link efficiency was performed by deriving the load impedance (Z_{MN}) (Equations 3.15 and 3.17) and the load quality factor (Q_L) (Equations 3.16 and 3.18) for both configurations. Note that the expressions are valid for any TX circuit topology employed [9].

$$Z_{\text{MN_SP}} = \frac{1}{R_L(\omega C_{\text{Rx}})^2} - \frac{j}{\omega C_{\text{Rx}}} \tag{3.15}$$

$$Q_{\text{L_SP}} = \frac{R_L}{\omega L_{\text{Rx}}} \tag{3.16}$$

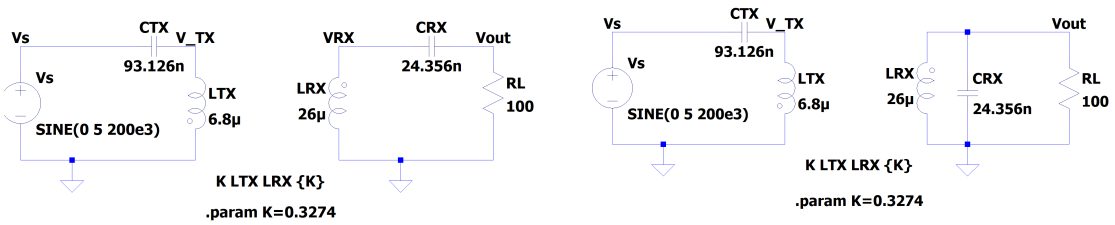
$$Z_{\text{MN_SS}} = R_L - \frac{j}{\omega C_{\text{Rx}}} \tag{3.17}$$

$$Q_{\text{L_SS}} = \frac{\omega L_{\text{Rx}}}{R_L} \tag{3.18}$$

- LTspice Validation: The analytical model was verified through LTspice simulations to evaluate the link efficiency (Equation 3.19) and the total system efficiency (Equation 3.20). The simulated schematics are shown in Figure 3.4.

$$\eta_{\text{Link}} = \frac{P_{\text{rx}}}{P_{\text{tx}}} \tag{3.19}$$

$$\eta_{\text{Tot}} = \frac{P_{\text{out}}}{P_{\text{in}}} \tag{3.20}$$



(a) Series-Series topology (b) Series-Parallel topology

Figure 3.4: Comparison between the (a) SS and (b) SP topologies

The comparative results of both the theoretical calculations and the LTspice simulations are summarized in Table 3.9.

Parameter	Series-Parallel (SP)	Series-Series (SS)
Analytical Calculations		
Load Impedance (Z_{MN})	10.67 Ω	100 Ω
Load Quality Factor (Q_L)	3.06	0.32
Theoretical Link Efficiency	85.34%	66.72%
LTspice Simulations		
Simulated Link Efficiency (η_{Link})	84.31%	63.92%
Simulated Total Efficiency (η_{Tot})	84.33%	66.88%

Table 3.9: Analytical and simulated performance comparison between SP and SS topologies under identical load conditions.

As demonstrated by the results, the theoretical predictions align with the simulations. The SP configuration outperformed the SS topology in these specific load conditions, yielding an efficiency improvement of approximately 20%. Consequently, the SP topology was selected and implemented as the final solution for the RX circuit.

3.5 Resonance Capacitance

Given the inductance values of the coils in Tables 3.6 and 3.7 , the ideal capacitance for the TX and RX required to achieve resonance at the target operating frequency of 200 kHz were calculated using Equation 3.21 and Equation 3.22.

$$C_{\text{TX}} = \frac{1}{(2\pi f)^2 \cdot L_{\text{TX}}} = 93.126\,\text{nF} \tag{3.21}$$

$$C_{\text{RX}} = \frac{1}{(2\pi f)^2 \cdot L_{\text{RX}}} = 24.356\,\text{nF} \tag{3.22}$$

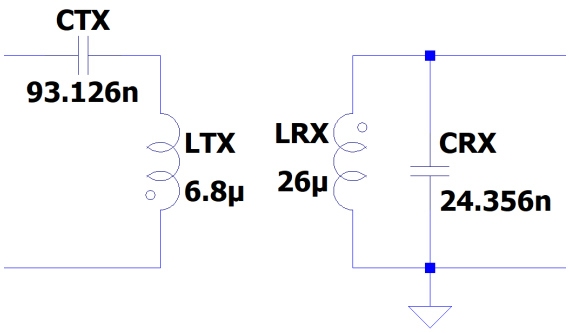


Figure 3.5: SP Resonance configuration

3.6 Matching Network

The design of the receiver matching network stage initially involved exploring various complex impedance matching network topologies, and in particular a low pass Low-high matching network, shown in Figure 3.6 .

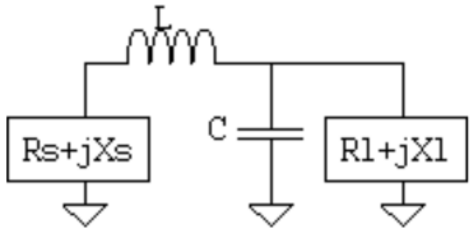


Figure 3.6: low pass Low-high matching network

However, through comprehensive simulation analyses, it was determined that implementing a dedicated multi-component matching network was unnecessary. Instead, the receiver architecture was simplified to utilize only a resonance capacitor connected across the receiving coil (Figure 3.7a)

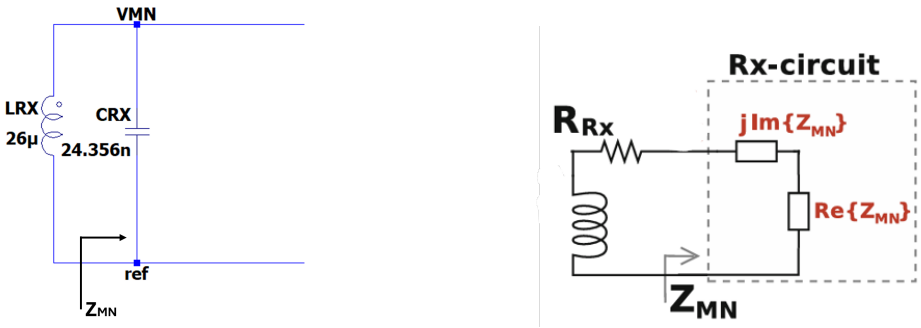
As previously explained in Section 2.4, the theoretical maximum link efficiency for this specific system requires an optimal matching impedance characterized by:

- $\Re\{Z_{\text{mn,opt}}\} = 15.7\ \Omega$
- $\Im\{Z_{\text{mn,opt}}\} =$ - 32.76 Ω (where $\Im\{Z_{\text{mn}}\} = -\omega L_{\text{rx}}$)

Through comprehensive LTspice simulation analyses utilizing only the parallel resonance capacitor, the resulting impedance values of the implemented circuit were evaluated as:

- $\Re\{Z_{\text{mn}}\} = 8.18\ \Omega$
- $\Im\{Z_{\text{mn}}\} =$ - 26.39 Ω

Although the simulated real part of the impedence does not perfectly match the theoretical calculations, these values represent a satisfactory compromise. The chosen simplified architecture provides impedance matching and maintains a high link efficiency, while minimizing the component count.



(a) Receiver circuit ZMN

(b) Theorical circuit schematic for reference.

Figure 3.7: Receiver matching network

3.7 Voltage Rectifier

To determine the optimal rectifying stage of the RX circuit, three rectifier topologies were evaluated: the voltage doubler, the full-bridge rectifier, and the Class E rectifier. An initial stand-alone performance analysis was conducted and the results of which are reported in Table 3.10.

Rectifier Topology	**Simulated Efficiency**
Voltage Doubler	90.9%
Full-Bridge	88.26%
Class E	82.43%

Table 3.10: Simulated stand-alone efficiencies of evaluated rectifier topologies

While the stand-alone analysis indicated that the voltage doubler achieved the highest efficiency, a comprehensive evaluation of the overall circuit led to different conclusions. The voltage doubler [23] utilizes a network of diodes and capacitors to both rectify the AC signal and double the peak output voltage. Although it achieved the highest stand-alone efficiency (90.9%), system-level simulations demonstrated that the voltage multiplication effect generated DC levels that exceeded the maximum input voltage thresholds of the following DC-DC converter (detailed in Section 3.8). Exceeding these limits could bring to the risk of irreversible damage to the components, rendering this topology unsuitable for the proposed architecture. The class E rectifier [24] is a resonant rectifier designed to achieve high efficiency by operating under zero-voltage or zero-current switching conditions and it generated a simulated stand-alone efficiency of 82.43%. However, it was discarded due to the unfeasible sizing of its required inductive component. Following the analytical design guidelines proposed in [24], calculations revealed an excessively high inductance value. Finally, the full-bridge rectifier [25] is a standard configuration which employs four diodes to provide full-wave rectification of the input AC signal without voltage multiplication. Other than achieving an efficiency of 88.26% in the stand-alone performance analysis, system-level simulations confirmed that, under the specific nominal conditions chosen for

this design phase, the full-bridge topology successfully maintains the rectified DC voltage safely below the critical input threshold of the DC-DC converter.

Consequently, the full-bridge topology shown in Figure 3.8 was ultimately selected for the final design.

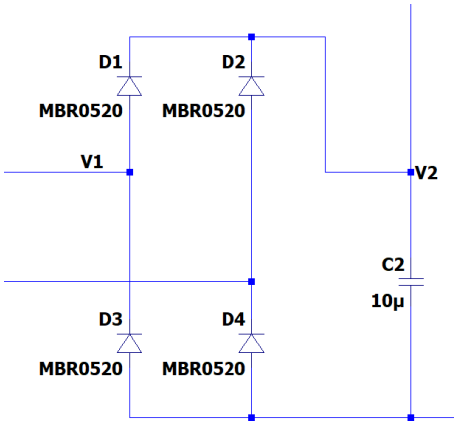


Figure 3.8: Full-bridge voltage rectifier

3.7.1 Diode selection

The diode bridge was implemented using MBR0520LT1G surface-mount Schottky power rectifiers [26]. This components were selected over standard alternatives, to satisfy the strict power efficiency and thermal constraints of the receiver.

The electrical specifications justifying this choice are detailed below:

- Minimized Conduction Losses: The MBR0520LT1G presents a low forward voltage drop (V_F) of 0.45V at the system's operating current. This minimizes conduction losses across the bridge.
- Reverse Voltage: The MBR0520LT1G offers a low reverse voltage rating ($V_R = 20$ V).
- Current Margins: The operating current of the MBR0520LT1G is around 500 mA, while other diodes are limited to a 70 mA maximum continuous forward current.

3.8 Power Supply and dual-rial supply generation

The primary objective of the power management stage is to satisfy the power demands of the Intan RHS2116 neurostimulator. As detailed in Section 3.1.1, this specific application requires a highly stable, regulated main power supply of +3.3 V, alongside a dual-rail supply (±3.3 V) necessary to drive the biphasic neural stimulation pulses. To meet these requirements, a two-stage power management architecture was implemented, employing the LTC3129-1 [27] and LTC660 [28] integrated circuits.

3.8.1 LTC31291-1 Buck-Boost Converter

The first stage of the power management network is the LTC3129-1, a monolithic synchronous buck-boost DC-DC converter. In the specific application of the WPT system, the rectified DC input voltage is unstable, due to possible coil misalignment, due to prosthetic shifting, or changing of the load conditions. The chosen component addresses these environmental variables through its buck-boost transition capabilities. This architecture allows the converter to regulate in both step-down and step-up modes, guaranteeing a stable +3.3 V output, thereby ensuring uninterrupted operation of the RHS2116 neurostimulator. Futhermore, operating with an exceptionally low quiescent current ($I_Q \approx 1.3\ \mu$A), the device maximizes power conversion efficiency across a wide range of load conditions. The LTC3129-1 converter presents a wide input voltage range (2.42V to 15V) and it is housed in a thermally enhanced 3x3 mm QFN package, ensuring efficient thermal management.

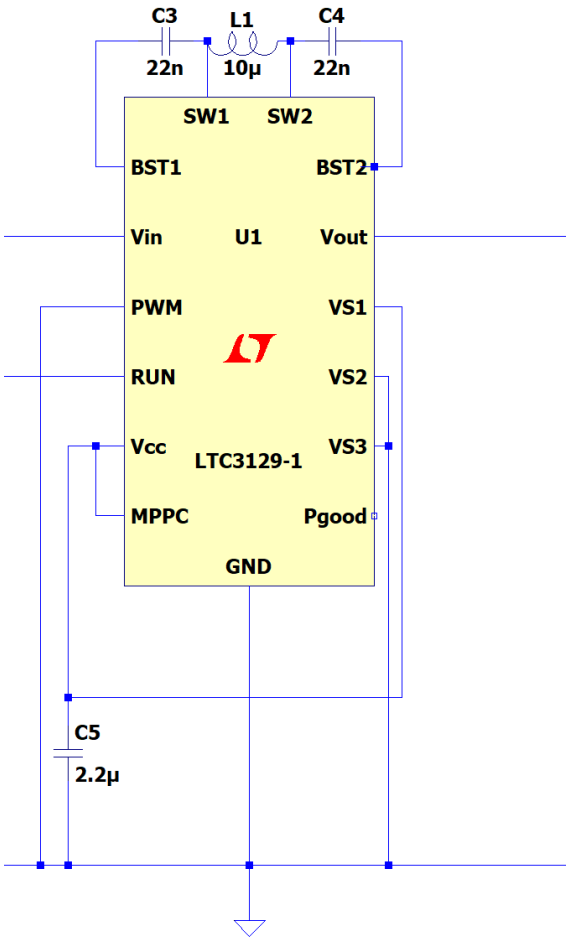


Figure 3.9: LTC3129-1 buck-boost converter.

The hardware configuration of the LTC3129-1 was specifically tailored to optimize efficiency. The specific pin choices, following the manufacturer's specifications [27], are detailed below:

- Mode Selection (PWM): The PWM pin was tied to ground. This configuration enables the converter's automatic Burst Mode operation. In this application, Burst Mode is advantageous as it maximizes power conversion efficiency during the low-power or standby states of the neurostimulator, thereby reducing quiescent current and minimizing continuous thermal dissipation.
- Power Good Indicator (PGOOD): The PGOOD pin was left unconnected, since external power sequencing or fault monitoring logic is not required for the RHS2116 in this architecture.
- Output Voltage Programming (VS1, VS2, VS3): To generate the required +3.3 V output the IC's internal voltage matrix was utilized. Following the manufacturer's

logic table, the VS3 and VS2 pins were connected to ground, while the VS1 pin was tied directly to the internal regulator voltage (V_{CC}).

3.8.2 LTC660

Since the Intan RHS2116 neurostimulator demands a negative rail, other than the positive +3.3V obtained in output of the LTC3129-1, to generate the symmetrical ±3.3 V dual-supply necessary for driving balanced biphasic pulses, to complete the power architecture required for neural stimulation, the LTC660 was chosen.

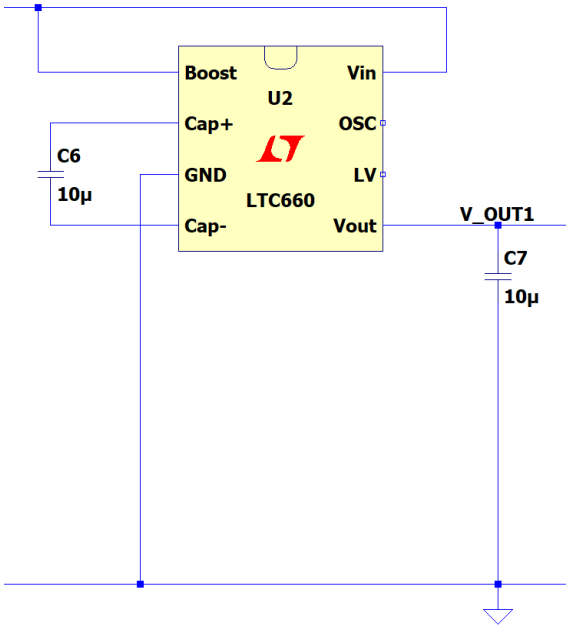


Figure 3.10: LTC660 voltage converter.

The LTC660 is a monolithic CMOS switched-capacitor voltage converter and it was selected for this role because it offers a highly efficient, inductorless solution to invert the positive +3.3 V input into a stable −3.3 V output. Furthermore, the device features high power conversion efficiency and low output resistance. [28],

Chapter 4

Validation through LTspice

4.1 Baseline design specifications

The initial circuit design was carried out based on chosen nominal baseline conditions, derived from the considerations regarding the power dissipation of the load, detailed in 3.1.2, and phyisical considerations:

- Nominal power consumption: 100 mW, representing the maximum operating power required by the RHS2116 neurostimulator during active neural stimulation tasks.
- Nominal inter-coil distance: 10 mm, approximating the spatial distance between coils in a standard condition, assuming the two coils perfectly aligned. This dimension accounts for the thickness of the tissues between the implanted RX coil and TX coil.

Based on the considerations above, the magnetic coupling coefficient (k) necessary for the preliminary design phase was analytically calculated using equation 2.6 [12], resulting in a baseline value of 0.3274.

To accurately evaluate the system's performance, the TX was modeled as an ideal LC resonant tank driven by a voltage source with a 1 V peak amplitude.

The correct functioning of the developed RX circuit was validated through circuit simulations performed in LTspice. Figure 4.1 shows the resulting RX circuit.

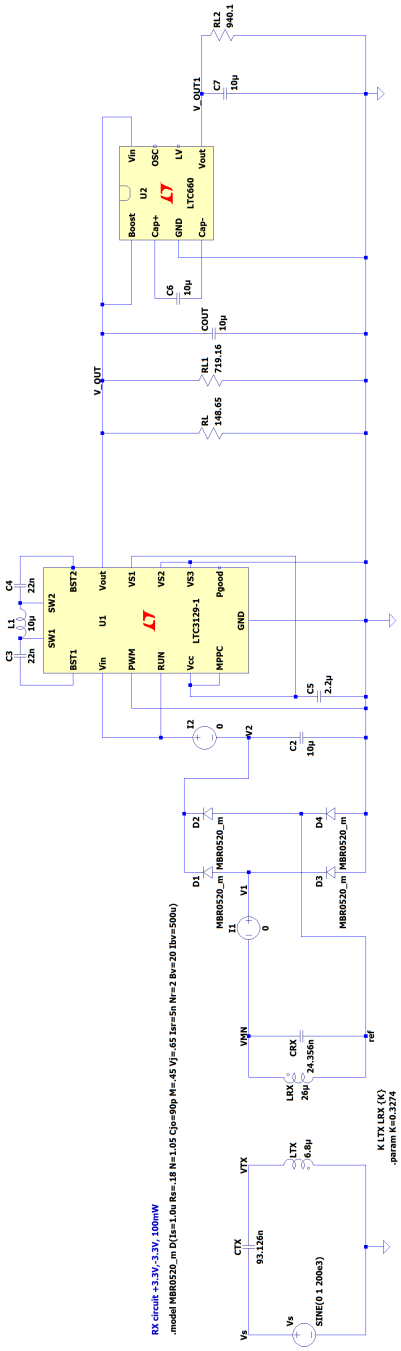


Figure 4.1: LTspice model of the Rx-circuit.

4.2 Testing

4.2.1 Power Consumption

The simulations evaluated the system behavior across three distinct power consumption scenarios, as previously defined in Section 3.1.2:

- 100 mW: The maximum design condition, representing peak power consumption, corresponding to the baseline conditions.
- 50 mW: The standard operating condition of the RHS2116 neurostimulator during active recording and stimulation.
- 30 mW: The minimum standard condition, corresponding to low-power or standby states.

The link efficiency (η_{link}) (4.1), rectification efficiency (η_{rect}) (4.2), DC-DC efficiency (η_{dcdc}) (4.3) and total system efficiency (η_{tot}) (4.4) were evaluated as follows to define the behavior of the circuit in the three load power consumption conditions:

$$\eta_{\text{link}} = \frac{P_{\text{rx}}}{P_{\text{tx}}} \tag{4.1}$$

$$\eta_{\text{rect}} = \frac{P_2}{P_1} \tag{4.2}$$

$$\eta_{\text{dcdc}} = \frac{P_{\text{out}}}{P_2} \tag{4.3}$$

$$\eta_{\text{tot}} = \frac{P_{\text{out}}}{P_{\text{tx}}} \tag{4.4}$$

With reference to Figure 4.1, the power variables are defined as follows:

- P_{tx} is the power measured at the Tx coil (Equation 4.5);
- P_{rx} is the power measured at the Rx coil (Equation 4.6);
- P_1 is the power measured at the input of the rectification block (Equation 4.7);
- P_2 is the power measured at the input of the LTC3129-1 DC-DC converter(Equation 4.8);
- P_{out} is the final power measured at the output of the LTC3129-1 DC-DC converter, calculated as shown in Equation 4.9.

It is important to note that all voltage and current variables used in these calculations were evaluated as Root Mean Square (RMS) values and measured only after the transient response had settled and the signals had reached steady-state convergence.

$$P_{\text{tx}} = V_{\text{tx}} \cdot I_{\text{tx}} \tag{4.5}$$

$$P_{\text{rx}} = V_{\text{rx}} \cdot I_{\text{rx}} \tag{4.6}$$

$$P_1 = V_1 \cdot I_1 \tag{4.7}$$

$$P_2 = V_2 \cdot I_2 \tag{4.8}$$

$$P_{\text{out}} = V_{\text{out}} \cdot I_{\text{out}} \tag{4.9}$$

The results in terms of power and efficiency performance are shown in Table 4.1.

Parameter	**Maximum Load**	**Standard Load**	**Minimum Load**
Transmitted Power (P_{tx})	151.88 mW	80.09 mW	55.06 mW
Received Power (P_{rx})	124.78 mW	59.48 mW	35.28 mW
Total Output Power (P_{tot})	99.81 mW	49.99 mW	30.05 mW
Link Efficiency (η_{link})	82.16%	74.26%	64.08%
Rectification Efficiency (η_{rect})	85.36%	89.16%	89.55%
DC-DC Efficiency (η_{dcdc})	83.06%	83.40%	84.11%
Total System Efficiency (η_{tot})	65.72%	62.42%	54.57%

Table 4.1: Power and efficiency performance of the WPT system across the three simulated load conditions.

An evaluation of the simulation results demonstrates robust performance across the three different load conditions.

Under the minimum load condition of 30 mW, the circuit shows satisfactory performance, with a wireless link efficiency (η_{link}) of 64.08% and a cumulative total system efficiency (η_{tot}) of 54.57%. In correspondence with the standard (50 mW) and maximum (100 mW) operating points, the link efficiency progressively improves, reaching an optimal peak of 82.16% and a total system efficiency of 65.72% under the maximum load condition.

Evaluating the stage-by-stage performance characteristics led to the following observations: both the rectification stage and the DC-DC conversion stage maintain stability across the three different load conditions, with the rectification efficiency ranging between 85.36% and 89.55%, and the DC-DC conversion efficiency remaining above 83%.

The overall results confirm that the proposed circuit architecture can successfully manage load fluctuations.

To further assess the correct functioning of the receiver circuit, the average DC input voltage ($V_{in,DCDC}$) was monitored across all three load conditions. The average DC input voltage values recorded during the LTspice simulations are summarized in Table 4.2.

Load Condition	**Average DC Input Voltage ($V_{in,DCDC}$)**
Maximum Load (100 mW)	3.70 V
Standard Load (50 mW)	4.73 V
Minimum Load (30 mW)	5.04 V

Table 4.2: Average DC input voltage to the DC-DC converter across the simulated load conditions.

As reported, the voltage ranges from 3.70 V at 100 mW up to a peak of 5.04 V at 30 mW. This satisfies the maximum input voltage limit imposed by the DC-DC converter specifications, remaining well below the maximum limit of 15 V and ensuring correct operation.

4.2.2 Coils Misalignment Analysis

To evaluate the robustness of the WPT link against spatial variations, a coil misalignment analysis was conducted. This analysis assumed a baseline power consumption of 100 mW. The coupling coefficient k was investigated as a function of both vertical distance variations (D) and angular misalignment (θ).

To quantify the sensitivity of the link, the resulting values of k were evaluated across different misalignment conditions, using the Equation 2.6 in Section 2.3.5. The impact of pure vertical distance displacement (at $\theta = 0°$) is summarized in Table 4.3, while Table 4.4 presents the combined effects of both distance and angular variations (15°, 30°, and 45°).

Distance (D)	**Coupling Coefficient (k)**
10 mm	0.3274
12 mm	0.2429
14 mm	0.1818
16 mm	0.1379
18 mm	0.1061
20 mm	0.0828

Table 4.3: Coupling coefficient k as a function of vertical distance D (at $\theta = 0°$).

Distance (D)	$\theta = 0°$	$\theta = 15°$	$\theta = 30°$	$\theta = 45°$
10 mm	0.3274	0.3162	0.2835	0.2315
12 mm	0.2429	0.2347	0.2104	0.1718
14 mm	0.1818	0.1756	0.1575	0.1286
16 mm	0.1379	0.1332	0.1194	0.0975

Table 4.4: Coupling coefficient k under combined vertical distance and angular misalignment (θ).

4.2.3 Vertical misalignment

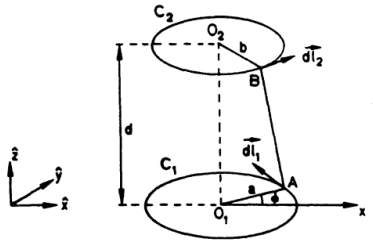


Figure 4.2: vertical misalignment[29]

To evaluate the impact of vertical misalignment (Figure 4.2) on the wireless power transfer performance, the system's efficiency stages and coupling coefficient were analyzed across a range of separation distances (d) from 12 mm to 20 mm. The results are summarized in Table 4.5.

Distance (d)	**Coupling** (k)	**Link Eff.** (η_{link})	**Rect. Eff.** (η_{rect})	**DC-DC Eff.** (η_{dcdc})	**Total Eff.** (η_{tot})
12 mm	0.2429	74.6%	90.8%	82.5%	63.0%
14 mm	0.1818	63.3%	93.4%	82.3%	54.9%
16 mm	0.1379	50.7%	94.2%	82.3%	44.3%
18 mm	0.1061	39.2%	94.3%	80.2%	33.5%
20 mm	0.0828	33.9%	74.7%	80.3%	22.9%

Table 4.5: System efficiency as a function of vertical distance D.

The average DC input voltage ($V_{in,DCDC}$) was monitored in correspondance to the different separation distances. The results are shown in Table 4.6.

Distance (d)	**Average DC Input Voltage** ($V_{\mathbf{in,\ DCDC}}$)
12 mm	6.32 V
14 mm	9.12 V
16 mm	12.35 V
18 mm	16.1 V
20 mm	19.7 V

Table 4.6: Average DC input voltage to the DC-DC converter across different transmission distances.

In this regard, further investigation revealed that the input voltage of the DC-DC converter (V_{in}) significantly increases due to a higher current in the TX coil, which is triggered by a reduction in the coupling coefficient (k).

Coupling Coefficient (k)	TX Current (I_{tx})	RX Voltage (V_{rx})	DC Input Voltage ($V_{\text{in, DCDC}}$)
0.3274	248.64 mA	2.56 V	2.56 V
0.2429	233.48 mA	3.15 V	6.31 V
0.1818	259.49 mA	4.55 V	9.12 V
0.1379	318.52 mA	6.2 V	12.35 V
0.1061	422.45 mA	8.02 V	16.1 V
0.0828	634.67 mA	12.3 V	19.71 V

Table 4.7: Correlation between coupling coefficient (k), transmitter current (I_{tx}), receiver voltage (V_{rx}), and DC input voltage ($V_{\text{in, DCDC}}$) during LTspice simulations.

In summary, the circuit architecture ensures safe operation within the DC-DC converter specifications for coil separation distances up to 16 mm. For distances exceeding this threshold, the system exhibits an average DC input voltage greater than 15 V. This poses a critical issue, as violating the maximum voltage limit can cause permanent damage to the component or lead to general system failure.

Regarding the system efficiency analysis, a minimum link efficiency of 50.7% and a corresponding total system efficiency of 44.3% are successfully maintained while keeping the operating parameters strictly within the input limits of the DC-DC converter.

4.2.4 Angular misalignment

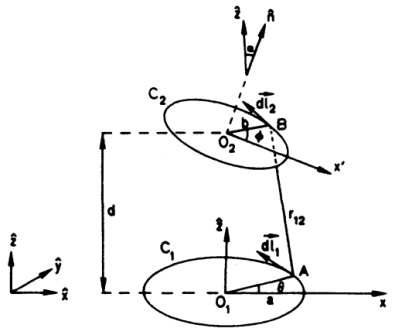


Figure 4.3: angular misalignment[29]

The effect of angular misalignment (Figure 4.3) was evaluated by testing angles of 15°, 30°, and 45° across four different vertical misalignment distances (10 mm, 12 mm, 14 mm, and 16 mm). The corresponding results are summarized in Tables 4.8, 4.9, 4.10, 4.11:

Misalignment Angle	Coupling Coefficient (k)	Link Efficiency (η_{link})	Rectifier Efficiency (η_{rect})	DC-DC Efficiency (η_{dcdc})	Total Efficiency (η_{tot})
0°	**0.3274**	82.1 %	85.8 %	83.1 %	**66.1 %**
15°	**0.3162**	81.6 %	85.4 %	83.7 %	**65.8 %**
30°	**0.2835**	79.1 %	88.1 %	83.3 %	**65.5 %**
45°	**0.2315**	72.9 %	91.5 %	82.4 %	**62.0 %**

Table 4.8: System efficiency evaluated at different misalignment angles at a fixed distance of $D = 10\,\text{mm}$.

Misalignment Angle	Coupling Coefficient (k)	Link Efficiency (η_{link})	Rectifier Efficiency (η_{rect})	DC-DC Efficiency (η_{dcdc})	Total Efficiency (η_{tot})
0°	**0.2429**	74.6 %	90.8 %	82.5 %	**63.0 %**
15°	**0.2347**	73.4 %	91.3 %	82.4 %	**62.3 %**
30°	**0.2104**	69.4 %	92.4 %	82.3 %	**59.5 %**
45°	**0.1718**	60.8 %	93.4 %	82.5 %	**52.9 %**

Table 4.9: System efficiency evaluated at different misalignment angles at a fixed distance of $D = 12\,\text{mm}$.

Misalignment Angle	Coupling Coefficient (k)	Link Efficiency (η_{link})	Rectifier Efficiency (η_{rect})	DC-DC Efficiency (η_{dcdc})	Total Efficiency (η_{tot})
0°	**0.1818**	63.3 %	93.4 %	82.3 %	**54.9 %**
15°	**0.1756**	61.8 %	93.4 %	82.4 %	**53.7 %**
30°	**0.1575**	56.9 %	93.4 %	82.8 %	**49.6 %**
45°	**0.1286**	47.5 %	94.5 %	82.0 %	**41.5 %**

Table 4.10: System efficiency evaluated at different misalignment angles at a fixed distance of $D = 14\,\text{mm}$.

Misalignment Angle	Coupling Coefficient (k)	Link Efficiency (η_{link})	Rectifier Efficiency (η_{rect})	DC-DC Efficiency (η_{dcdc})	Total Efficiency (η_{tot})
0°	**0.1379**	50.7 %	94.2 %	82.3 %	**44.3 %**
15°	**0.1332**	49.1 %	94.3 %	82.2 %	**42.9 %**
30°	**0.1194**	44.2 %	95.0 %	81.1 %	**38.4 %**
45°	**0.0975**	36.2 %	91.8 %	80.2 %	**30.0 %**

Table 4.11: System efficiency evaluated at different misalignment angles at a fixed distance of $D = 16\,\text{mm}$.

The average DC input voltage ($V_{in,DCDC}$) values measured under the various simulated conditions are reported in Table 4.12.

Vertical Distance	**Angular Misalignment**			
	0°	**15°**	**30°**	**45°**
10 mm	3.7 V	4.1 V	5.0 V	6.5 V
12 mm	6.3 V	6.5 V	7.6 V	9.5 V
14 mm	9.1 V	9.4 V	10.6 V	13.2 V
16 mm	12.4 V	13.2 V	14.2 V	17.1 V

Table 4.12: Average DC input voltage ($V_{\text{in, DCDC}}$) evaluated across different vertical distances and angular misalignments.

At distances of 10 mm and 12 mm, any angular misalignment remains well within the DC-DC converter's safety margins, ensuring the system does not exceed the allowed voltage tolerances during standard operation. At a distance of 14 mm, the system remains in the limits; however, at a misalignment of 45°, it operates dangerously close to the maximum input voltage limit, potentially compromising the correct functioning of the circuit.

At the distance of 16 mm, the system only operates safely up to a 30° misalignment, at which point it approaches the maximum input limit. Beyond this, at a 45° misalignment, the input voltage exceeds the DC-DC converter's absolute maximum voltage limit, risking permanent component damage and total system failure.

Regarding overall system performance, the total efficiency decreases as distance and angular misalignment increase. However, the isolated efficiency of the rectifier stage shows an upward trend under these same conditions.

Chapter 5

PCB design and testing

5.1 PCB design

Following the theorical design analysis and the LTspice validation, the physical implementation of the receiver's Printed Circuit Board (PCB) was carried out using Altium Designer. The PCB layout strategy focused on the following critical design considerations, establishing a balance between electrical performance and miniaturization:

- 2-Layer Stack-Up: A two-layer configuration was selected for this prototype. This approach resulted optimal for the definition of an initial prototype, avoiding the unwanted parasitics often introduced by a multi-layer stack up.
- Miniaturization: The board was designed to achieve a compact dimension by selecting small-package components, resulting in overall dimensions of 62 mm x 30 mm. While these dimensions are not yet suitable for implantation in-body, the expanded size allows for convenient testability and visual inspection. In future work, the PCB will certainly undergo miniaturization to safely fit within the electronics housing located in the tissue.
- Modularity: Dedicated pin headers were inserted at the input for secure connection to the receiver coil, and at the output for load connection and reliable signal extraction. Moreover, additional headers were placed on the control pins of the DC-DC converters to allow potential configuration changes during experimental testing. Specifically, these headers can enables manual switching of the PWM and PGOOD pins on the LTC3129-1, as well as the OSC and LV pins on the LTC660.
- Optimization: Trace widths in the AC section of the board were significantly enlarged. This safety measure was taken to handle Radio Frequency (RF) currents, minimize equivalent series resistances, and reduce power losses.

The PCB electrical schematic is shown in Figure 5.1 and the PCB final layout in Figure 5.2.

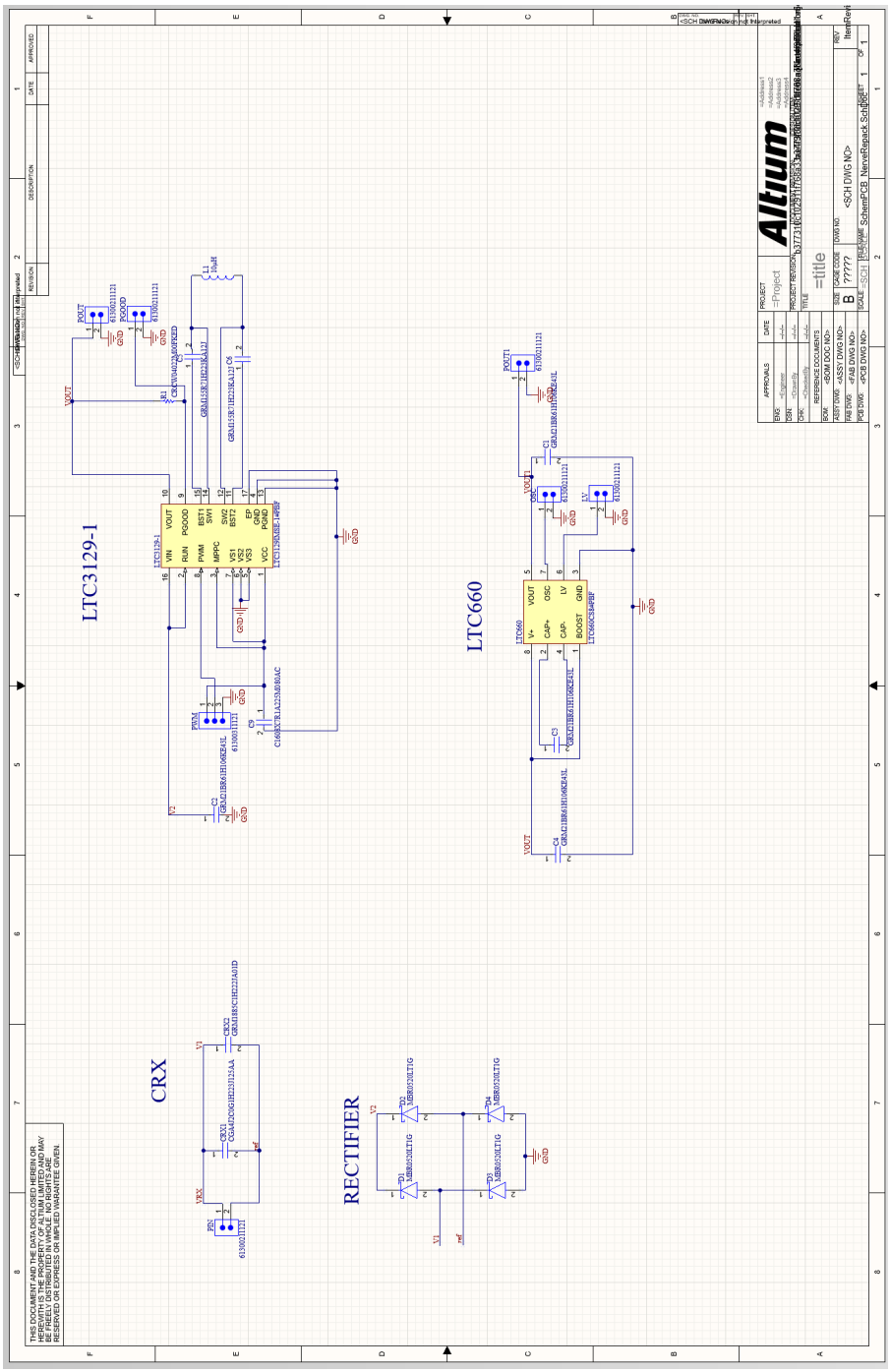
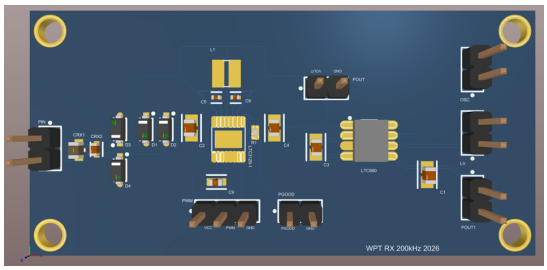
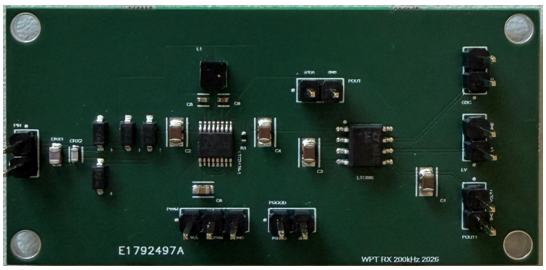


Figure 5.1: Altium designer schematic



(a) Rx circuit board 3D layout



(b) Rx circuit PCB

Figure 5.2: PCB layout

5.2 Testing

5.2.1 LTC4125 DEMO CIRCUIT 2773A-A-KIT

For testing, the LTC4125 DEMO CIRCUIT 2773A-A-KIT was used. The LTC4125 transmitter employs an Auto Resonant drive mechanism to maximize power transfer, monitoring the current in the transmit tank using an internal zero-crossing detector. This data is used by an auto-feedback loop to fix the driving frequency, ensuring that it perfectly matches the natural resonant frequency of the LC circuit. Furthermore, the tank is driven by a square wave with a duty cycle of less than 50% , which maintains optimal efficiency regardless of environmental variations or coupling changes. [30]. The performance summary of the board is shown in Figure 5.4.

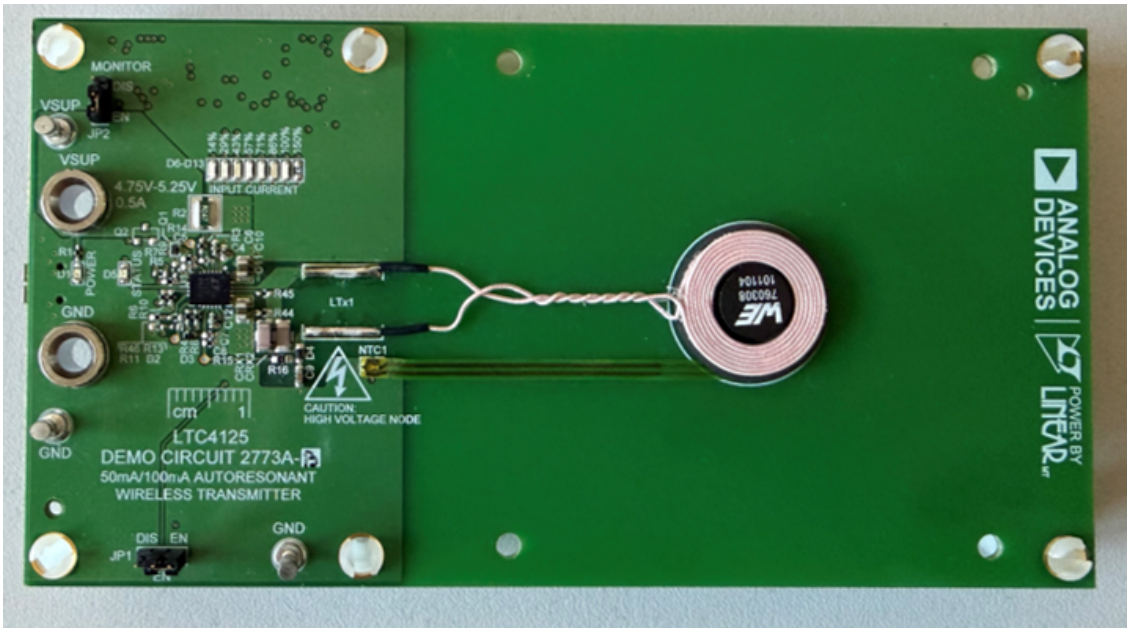


Figure 5.3: LTC4125 DEMO CIRCUIT 2773A-A-KIT

SYMBOL	PARAMETER	CONDITIONS	MIN	TYP	MAX	UNITS
V_{IN}	DC2773A-A Voltage Input	$I_{VIN} \leq 500mA$	4.5		5.5	V
I_{IN}	DC2773A-A V_{IN} Current	$V_{IN} = 5V$			500	mA
V_{BAT}	DC2775A-C Battery Charge Voltage	V_{SEL1} = HI, V_{SEL2} = HI		4.35		V
		V_{SEL1} = HI, V_{SEL2} = LO		4.20		V
		V_{SEL1} = LO, V_{SEL2} = HI		4.1		V
		V_{SEL1} = LO, V_{SEL2} = LO		4.00		V
I_{BAT}	DC2775A-C Charge Current	V_{BAT} = 4.0V, $I_{SEL1} = V_{CC}$, I_{SEL2} = GND		50		mA
AIR-GAP	Separation Between L_{TX} and L_{RX} Coils		3	3.5	5	mm
f_{TX_TANK}	DC2773A-A Resonant Tank Frequency			200		kHz
f_{RX_TANK}	DC2775A-C Resonant Tank Frequency			200		kHz

Figure 5.4: LTC4125 DEMO CIRCUIT 2773A-A-KIT specifications [30]

5.2.2 Tests setup

The WPT system was initially tested by coupling the transmitter (TX) and receiver (RX) coils, utilizing the LTC4125 DEMO CIRCUIT 2773A-A-KIT as the transmission stage. The WE 60308101214 RX coil was connected to the receiver circuit board through the input headers, as shown in Figure 5.5 As a preliminary testing phase, the receiver was connected to the load corresponding to a power consumption of 100mW, in accordance with the values reported in Section 3.1.2. Moreover, the vertical distance between the two coils was set at 4mm, considering the limitation imposed by the manufacturer, which indicates a maximum distance between coils of 5mm. The experimental set up is shown in Figures 5.5 and 5.6. Following the manufacturer specifications illustrated in Figure 5.3, the input voltage (V_{IN}) was set to 5 V, resulting in an input current (I_{IN}) of 39 mA and a total input power (P_{IN}) of 195 mW.

System Stage	Parameter	Value
TX (LTC4125)	Input Voltage (V_{IN})	**5.0 V**
	Input Current (I_{IN})	**39 mA**
	Input Power (P_{IN})	**∼195 mW**
RX Circuit	Output Voltage (V_{OUT})	**+3.27 V**

Table 5.1: Measured parameters for the TX and RX stages.

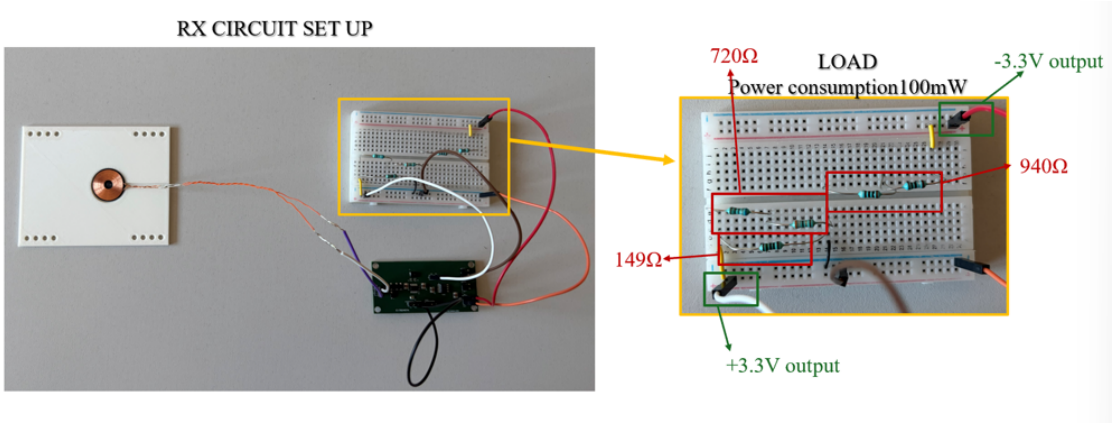


Figure 5.5: Rx circuit test set up

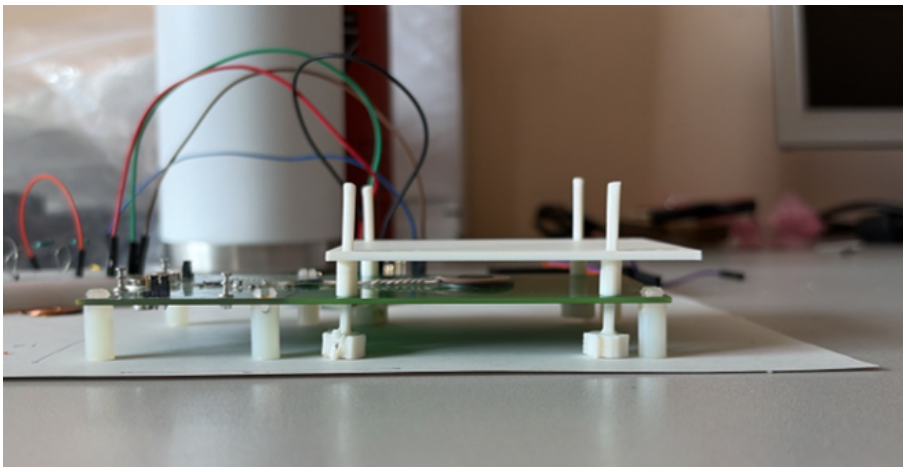


Figure 5.6: vertical disalignment set up

After an initial successful acquisition, the system failed to provide the expected output voltage. It is highly likely that the initial TX transmission delivered excessive power, overstressing the receiver circuit components.

5.2.3 Stand-Alone Receiver Circuit Investigation

To assess the cause of the failure, it was decided to bypass the receiving coil and directly evaluate the stand-alone circuit behavior. The RX board was disconnected from both the receiver coil and the load and a DC power supply was then connected directly to the VMN and REF input pins, applying a 4V DC input voltage to the circuit. The test set-up is shown in Figure 5.7.

The power supply successfully activated both the LTC3129-1 and LTC660 DC-DC converters. Output measurements confirmed the generation of +3.21 V and -3.21 V supply rails, which closely approximate the expected ±3.3 V target. However, a critical issue emerged regarding input current and input power, which were excessively high compared to the values obtained during the simulations.

Parameter	Set Value	Actual Measured Value
Voltage	4.000 V	3.252 V
Current	250 mA	248 mA
Power	-	∼806.5 mW

Table 5.2: Comparison between set parameters and actual measured values.

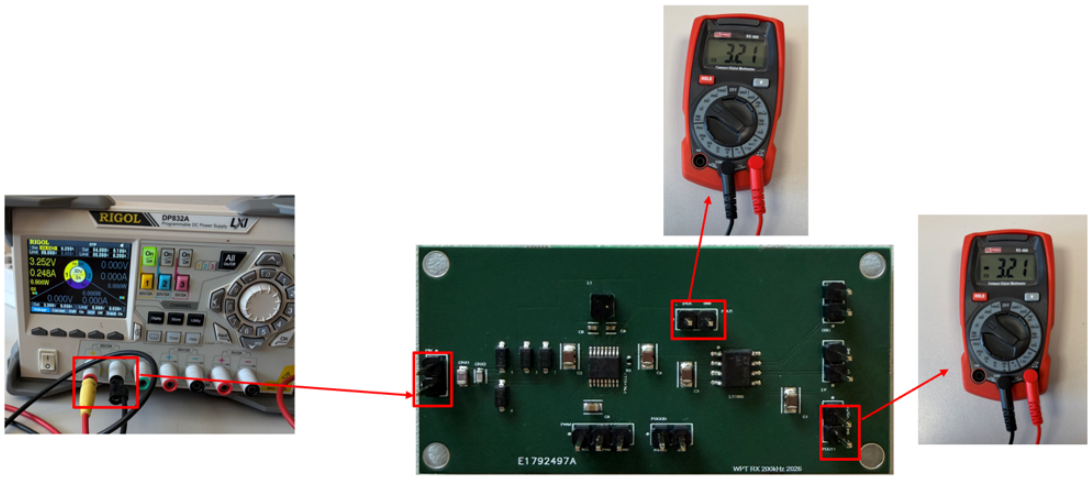


Figure 5.7: Rx circuit test set up - stand alone testing

To identify the compromised components, a Fluke thermal imaging camera was used for inspection. The thermal analysis revealed that the compromised component was the LTC3129-1, which exhibited excessive heat, likely reaching critical thermal conditions.

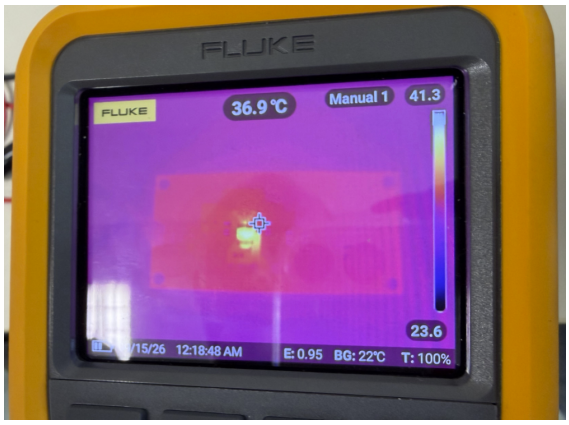


Figure 5.8: Fluke measurements

5.2.4 Stand-Alone Receiver Rectification Stage Investigation

To proceed with the troubleshooting, to verify the power transfer to the load and to check the output voltage of the rectification stage, the LTC3129-1 was desoldered from the PCB. An equivalent load resistance of approximately $1k\,\Omega$ was connected to the output of the full-bridge rectifier. The initial set-up utilizing the LTC4125 DEMO CIRCUIT 2773A-A-KIT was then reproduced, resulting in a measured output voltage of 6.5V, meaning correct power transfer from the transmitter to the receiver. Moreover, the value obtain is well below the input maximum voltage limit imposed by the LTC3129-1. The test set-up is showed in Figure 5.10, while the results of the acquisition are shown in Table5.3.

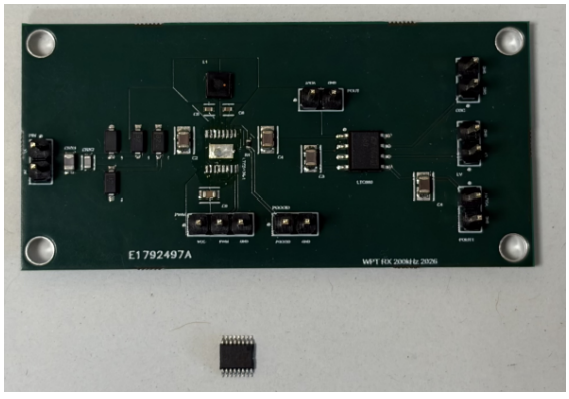


Figure 5.9: PCB - desoldered LTC3129-1

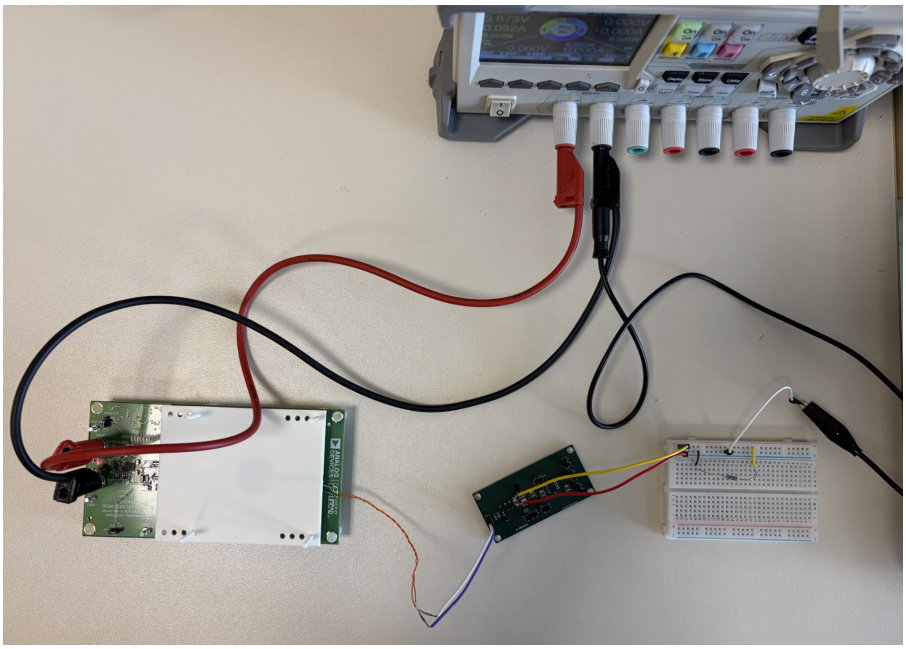


Figure 5.10: Test set up - stand-alone rectification stage testing

System Stage	Parameter	Value
TX (LTC4125)	Input Voltage (V_{IN})	**5.5 V**
	Input Current (I_{IN})	**37 mA**
	Input Power (P_{IN})	**∼203 mW**
RX Circuit	Rectifier Output Voltage (V_{OUT})	**+6.5 V**

Table 5.3: Measured parameters stand-alone recitification stage

Conclusions and future perspectives

5.3 Conclusions and Experimental Challenges

This thesis presented the modeling, design, and performance evaluation of a Near-Field Inductive Coupling (NIC) Wireless Power Transfer (WPT) receiver, specifically optimized to operate at a resonant frequency of 200 kHz. In accordance with the project specifications dictated by NerveRepack, the proposed architecture successfully achieved the target electrical requirements in a simulated environment, effectively delivering a stable +3.3 V voltage supply alongside a ±3.3 V dual-rail supply for the neural stimulation task of the RHS2116, demonstrating satisfactory efficiency levels.

LTspice simulations validated the robustness of the designed circuit. The system was evaluated under three power consumption conditions to simulate real-world load fluctuations. Even under the minimum load condition, the system maintained a link efficiency of 64.08% and a total system efficiency of 54.57%. Optimal performance was achieved at a maximum nominal load of 100 mW, reaching a peak link efficiency of 82.16% and a total efficiency of 65.72%.

Furthermore, the system demonstrated satisfactory misalignment tolerance across most standard operating conditions, maintaining the receiver's rectified input voltage within the 2.42 V to 15 V operational window of the LTC3129-1 DC-DC converter. However, under specific spatial displacement conditions, the input voltage of the DC-DC converter exceeded the maximum input voltage limit, resulting in possible component damage and system failure.

During the physical validation phase, hardware limitations were encountered. The primary issue was the reliance on the LTC4125 DEMO CIRCUIT 2773A-A-KIT. This board lacks the ability to control the input power manually, which made it unfeasible to reproduce and validate the conditions simulated in LTspice. In addition, the circuit suffered component damage, probably due to excessive supplied voltages, which induced overheating to the LTC3129-1.

5.4 Future Perspectives

To address the experimental challenges encountered and test the overall reliability of the designed circuit, the following future developments are proposed:

- Component Replacement: The permanently damaged LTC3129-1 chip must be replaced on the receiver PCB to restore full circuit functionality.
- Custom Transmitter Implementation: To proceed safely with empirical testing, the LTC4125 DEMO CIRCUIT 2773A-A-KIT should be replaced with a custom-designed LTC4125 transmitter board ([31]), which allows regulation of the emitted power, enabling faithful reproduction of the testing conditions evaluated in the simulation environment.
- Comprehensive Testing: Once the custom transmitter is integrated, the system can undergo experimental testing to evaluate its performance across the varying load and spatial misalignment conditions.

Moreover, several crucial developments are required to transition the prototype into a viable implantable device.

- Testing: The current experimental setup was thought to be conducted in air. Future iterations must evaluate the system's performance considering the electromagnetic attenuation and conductivity effects caused by biological tissue. Subsequent testing phases should be conducted using phantoms or ex-vivo animal models.
- Load Testing with the RHS2116 Chip: The receiver's performance has been evaluated using a equivalent resistive load. A critical future development will involve coupling the WPT receiver with the actual RHS2116 chip to evaluate the circuit response.
- Miniaturization: The current PCB dimensions must be reduced to safely fit within the restricted electronics housing of the implantation site, minimizing surgical invasivness.
- Refined System-Level Simulations: The current design phase and LTspice validations were conducted assuming an idealized transmitter circuit model, which was necessary to isolate and optimize the receiver's performance. Future optimized simulations should integrate a fully comprehensive equivalent circuit of the actual transmitter. Moreover, the system bust be tested considering the full electronics, the microcontroller and the control loop.

Bibliography

[1] S. R. Khan, S. K. Pavuluri, G. Cummins, and M. P. Y. Desmulliez, "Wireless Power Transfer Techniques for Implantable Medical Devices: A Review,".

[2] NerveRepack Project, "NerveRepack Official Website." [Online]. Available: https://www.nerverepack.eu/.

[3] A. Singer and J. T. Robinson, "Wireless power delivery techniques for miniature implantable bioelectronics," *Adv. Healthcare Mater.*, vol. 10, no. 17, p. 2100664, 2021.

[4] Wireless Power Transfer Charging System for AIMDs and Pacemakers Tommaso Campi, Silvano Cruciani, Federica Palandrani, Valerio De Santis, Senior Member, IEEE, Akimasa Hirata, Senior Member, IEEE, and Mauro Feliziani, Senior Member, IEEE

[5] Active Implantable Medical Device. Part 1: General Requirements for Safety, Marking and Information to be Provided by the Manufactures, CEN EN 45502-1, 1997.

[6] Designing Efficient Inductive Power Links for Implantable Devices Reid R. Harrison Department of Electrical & Computer Engineering University of Utah Salt Lake City, UT 84112 harrison@ece.utah.edu

[7] B. H. Waters, A. P. Sample, P. Bonde, and J. R. Smith, "Powering a ventricular assist device (VAD) with the free-range resonant electrical energy delivery (FREE-D) system," *Proc. IEEE*, vol. 100, no. 1, pp. 138–149, 2012, doi: 10.1109/JPROC.2011.2165309.

[8] IEEE, *IEEE Standard for Safety Levels with Respect to Human Exposure to Radio Frequency Electromagnetic Fields, 3 kHz to 300 GHz*, IEEE Std C95.1-2019, 2019.

[9] P. Pérez-Nicoli, F. Silveira, e M. Ghovanloo, *Inductive Links for Wireless Power Transfer: Fundamental Concepts for Designing High-Efficiency Wireless Power Transfer Links*, 1st ed., Cham, Switzerland: Springer, 2021.

[10] T.HLee,PlanarMicrowaveEngineering:APracticalGuide toTheory,Measurement, and Circuits,vol.1(CambridgeUniversityPress,2004)

[11] Impedans Ltd., "The L-Shaped Matching Network." [Online]. Available: `https://www.impedans.com/the-l-shaped-matching-network/`. Accessed: Jul. 15, 2026.

[12] A. Dentis, *Wireless Charging and Power Management System for Biomedical Implantable Devices*, Master's thesis, Politecnico di Torino, July 2023.

[13] G. L. Barbruni, P. Motto Ros, D. Demarchi, S. Carrara, and D. Ghezzi, *Miniaturised Wireless Power Transfer Systems for Neurostimulation: A Review*, IEEE Transactions on Biomedical Circuits and Systems, vol. 14, no. 6, pp. 1160–1178, Dec. 2020. doi: 10.1109/TBCAS.2020.3038599.

[14] J. P. Wright *et al.*, "A fully implantable wireless bidirectional neuromodulation system

for mice," *[Inserisci Nome Rivista]*, vol. [Vol], no. [Num], pp. [Pagine], [Anno].

[15] Intan Technologies, *RHS2116 Digital Electrophysiology Stimulator/Amplifier Chip Datasheet*, 2016 (updated 2021). Available: `http://intantech.com/files/Intan_RHS2116_datasheet.pdf`.

[16] J. P. Wright, I. T. Mughrabi, J. Wong, J. Mathew, N. Jayaprakash, and C. Crosfield, "A fully implantable wireless bidirectional neuromodulation system for mice," *Biosens. Bioelectron.*, vol. 200, p. 113919, 2022.

[17] S. Lienemann, M. J. Donahue, J. Zötterman, S. Farnebo, and K. Tybrandt, "A Soft and Stretchable Multielectrode Cuff for Selective Peripheral Nerve Stimulation," *Adv. Mater. Technol.*, vol. 8, no. 6, p. 2201322, 2023.

[18] F. Zurita *et al.*, "Thermoformed Parylene-C Cuff Electrodes for Small Nerve Interfacing," *Adv. Healthcare Mater.*, vol. 13, no. 1, p. 2302302, 2024.

[19] A. Carnicer-Lombarte *et al.*, "Implantable bioelectronics for gut electrophysiology," *Nat. Commun.*, vol. 16, 2025.

[20] G. Navarra, *Design and Development of Inductive Wireless Power Receivers for Implantable Neural Interfaces*. Master's thesis, Politecnico di Torino, Corso di laurea magistrale in Ingegneria Biomedica, 2026.

[21] Würth Elektronik, "WE-WPCC Wireless Power Charging Receiver Coil - 760308101214," *Datasheet*, 2023. [Online]. Available: https://www.we-online.com/

[22] Würth Elektronik, "WE-WPCC Wireless Power Charging Transmitter Coil - 760308101104," *Datasheet*, 2023. [Online]. Available: https://www.we-online.com/

[23] M.-D. Wei and R. Negra, "Voltage-Double RF Rectifier using Inductive Matching Network," in *2019 IEEE Wireless Power Transfer Conference (WPTC)*, London, UK, 2019, pp. 591–594.

[24] J. A. Santiago-González, K. M. Elbaggari, K. K. Afridi, and D. J. Perreault, "Design of Class E Resonant Rectifiers and Diode Evaluation for VHF Power Conversion," *IEEE Transactions on Power Electronics*, vol. 30, no. 9, pp. 4960–4972, Sept. 2015.

[25] Advancements in Inductive Wireless Power Transfer: A Comprehensive Review* Avishek Munsi* , Sushan Pradhan and Kunwar Aditya (Transportation Electrification Lab, Indian Institute of Technology Jodhpur, Jodhpur 342037, India)

[26] Micro Commercial Components (MCC), *MBR0520 THRU MBR0580 – 0.5 Amp Schottky Rectifier, 20 to 80 Volts*, Datasheet, Rev. 3-1-01012019, 2019. Disponibile online: `https://datasheet.lcsc.com/datasheet/pdf/864114c7268de3b1c0a20d2a90d4f676.pdf`.

[27] Analog Devices, *LTC3129-1 – 15V, 200mA Synchronous Buck-Boost DC/DC Converter with 1.3µA Quiescent Current*, Data Sheet, 29 October 2015. Disponibile online: `https://www.analog.com/en/products/ltc3129-1.html`.

[28] Analog Devices, *LTC660 – 100mA CMOS Voltage Converter*, Data Sheet, 24 August 2007. Disponibile online: `https://www.analog.com/media/en/technical-documentation/data-sheets/660fa.pdf`.

[29] M. Soma, D. C. Galbraith, and R. L. White, *Radio-Frequency Coils in Implantable Devices: Misalignment Analysis and Design Procedure*, IEEE Transactions on Biomedical Engineering, vol. BME-34, no. 4, pp. 276–282, Apr. 1987.

[30] Analog Devices, *LTC4124/LTC4125, 50mA Wireless Li-Ion Charger Demonstration Kit*, Demo Board Manual DC2770A, 2020. [Online]. Available: https://www.analog.com/

[31] H. Toloza, *Development of a Miniaturized BLE-Enabled Transmitter for Wireless Charging of Active Implantable Medical Devices*. Master's thesis, Politecnico di Torino, ANNO. Supervisors: Prof. Danilo Demarchi, Ph.D. Paolo Motto Ros, M.Sc. Fabiana Del Bono.